

# Generalized Analysis and Unified Design of *EM* Skins

G. Oliveri,<sup>(1)(2)</sup> M. Salucci,<sup>(1)(2)</sup> and A. Massa,<sup>(1)(2)(3)(4)</sup>

<sup>(1)</sup> *ELEDIA Research Center (ELEDIA@UniTN - University of Trento)*

DICAM - Department of Civil, Environmental, and Mechanical Engineering

Via Mesiano 77, 38123 Trento - Italy

E-mail: { *giacomo.oliveri, marco.salucci, andrea.massa* }@unitn.it

Website: *www.eledia.org/eledia-unitn*

<sup>(2)</sup> *CNIT - "University of Trento" ELEDIA Research Unit*

Via Sommarive 9, 38123 Trento - Italy

Website: *www.eledia.org/eledia-unitn*

<sup>(3)</sup> *ELEDIA Research Center (ELEDIA@UESTC - UESTC)*

School of Electronic Engineering, Chengdu 611731 - China

E-mail: *andrea.massa@uestc.edu.cn*

Website: *www.eledia.org/eledia-uestc*

<sup>(4)</sup> *ELEDIA Research Center (ELEDIA@TSINGHUA - Tsinghua University)*

30 Shuangqing Rd, 100084 Haidian, Beijing - China

E-mail: *andrea.massa@tsinghua.edu.cn*

Website: *www.eledia.org/eledia-tsinghua*

***This work has been submitted to the IEEE for possible publication. Copyright may be transferred without notice, after which this version may no longer be accessible.***

# Generalized Analysis and Unified Design of *EM* Skins

G. Oliveri, M. Salucci, and A. Massa

## Abstract

A generalized formulation is derived for the analysis of the field manipulation properties of electromagnetic skins (*EMSs*) in the working regimes of interest for wireless communications. Based on such a theoretical framework, a unified method for the design of anomalous-reflecting and focusing *EMSs* is presented. Representative results, from a wide set of numerical experiments, are reported and validated with full-wave *HFSS* simulations to give the interested readers some insights on the accuracy, the effectiveness, and the computational efficiency of the proposed analysis/synthesis tools.

**Key words:** Static Passive *EM* Skins; Inverse Scattering; Inverse Problems; Smart Electromagnetic Environment; *EM* Holography; Next-Generation Communications; Metamaterials, Metasurfaces.

# 1 Introduction and Motivation

The methodological approaches commonly adopted for designing wireless systems are currently subject to a deep revisiting due to the recent introduction of the Smart ElectroMagnetic Environment (*SEME*) paradigm [1]-[8] where the *propagation environment* is no longer an uncontrollable “element” of the wireless system that affects/limits its performance, but it can be actually profitably exploited by the designer [1][4][5]. Towards this end, suitable wave manipulating devices such as the static-passive *EMSs* (*SP-EMSs*) or the reconfigurable-passive *EMSs* (*RP-EMSs*), called reconfigurable intelligent surfaces (*RISs*), as well, have been introduced [1][4][5] and non-negligible improvements in the performance of the wireless system have been already demonstrated in several applicative areas including communications [1]-[4][9], sensing [10], and wireless power transmission [11].

It is worth pointing out that the use of *EMSs* (i.e., both static and reconfigurable non-amplifying structures) has been proposed to improve the wireless coverage and the quality-of-service (*QoS*), while minimizing the energy requirements and the needs, in terms of network architecture and protocols, for their integration within the wireless infrastructure [4]-[7]. On the other hand, passive reflecting structures can only redirect the wireless energy they collect [4][5], thus *EMSs* with electrically-large apertures are necessary in many applicative scenarios [10][12]-[14] to gather/deliver a sufficient amount of power.

Since the far-field (*FF*) region of any electromagnetic (*EM*) device starts at a distance proportional to the square of its size [15], *EMSs* with apertures of hundreds of wavelengths will often serve receiver terminals located in the Fresnel region [i.e., the so-called radiative near-field (*R-NF*)] [10][12]-[14]. Therefore, the extension/generalization of the formulation derived for *FF* conditions [16] has been recently considered for a reliable *EM* prediction of the *EMSs* behaviour. For instance, asymptotic path loss formulas have been derived for *R-NF/FF* cases [14], while closed-form approximations to determine the ergodic capacity of *R-NF/FF RIS*-aided wireless communication systems have been defined [13]. Furthermore, the exploitation of the *R-NF* properties of reflecting panels has been investigated in [10] to yield a robust localization. The impact of the *NF* focusing on the cumulative distribution function of the *NF* gain of *RISs* has been also evaluated by means of a phase-control strategy based on ideal spherical

wavefronts radiated by each meta-atom of the *RIS* [12]. However, to the best of the authors' knowledge, no rigorous and complete *EM*-based derivation is still available for (i) a generalized method for the analysis of the field manipulation properties of large *EMSs* in the working regimes of interest for wireless communications (i.e., the *R-NF* and the *FF* regions) starting from their micro-scale properties (i.e., the electric and magnetic surface currents as controlled by the local susceptibility of the *EMS* [17]) and for (ii) the physically-driven synthesis of large *EMSs*.

This paper is then aimed at complementing previous state-of-the-art works on the topic [10][12]-[14][16] (i) to derive rigorous yet simple expressions for the *EM* field reflected by large *EMSs* in both the *R-NF* and the *FF* regions, hence extending/generalizing the existing approaches in the *SEME* literature only based on *FF* approximations [5][16][17], (ii) to introduce a unified design approach for the synthesis of *EMSs*<sup>(1)</sup> in wireless communications, and (iii) to prove the advantages, in terms of power focusing, of using such a unified strategy when considering different setups, *EMS* apertures, transmitting/receiving antennas, distances, and *Snell* or *anomalous* (i.e., *Non-Snell*) directions of reflection of the impinging wave.

The main methodological innovations of the proposed work with respect to the state-of-the-art include:

- the derivation and the validation of a generalized analytic expressions for the *EM* field reflected by arbitrary *EMSs* used in wireless communications, which is based on the *Generalized Sheet Transition Condition (GSTC)* theoretical framework [17];
- the introduction of a unified method for the design of anomalous-reflecting wave manipulating devices used in wireless communications;
- the numerical assessment, also against commercial full-wave simulators (i.e., *Ansys HFSS* [18]), of the reliability of the generalized analysis method and of the effectiveness of arising synthesis approach.

The outline of the paper is as follows. After the generalization of the method for the analysis of the *EM* radiation from *EMSs* to include all the working conditions of interest for wireless

---

<sup>(1)</sup>As a matter of fact, the derived theory applies regardless of the meta-atom technology (i.e., static or reconfigurable passive unit cells). For the sake of simplicity, the numerical validation will refer to *SP-EMSs*.

communications (Sect. 2), a unified technique for the synthesis of arbitrary *EMS*s is derived and detailed in Sect. 3. A set of representative results from an exhaustive numerical analysis is presented and discussed in Sect. 4, also in comparison with full-wave simulations, to illustrate the features and to assess the reliability of the proposed theoretical formulation as well as to provide some insights on the effectiveness and the computational efficiency of the arising *EMS* design method. Some concluding remarks follow (Sect. 5).

## 2 Generalized *EMS*-Analysis

Let us consider the reference scenario in Fig. 1(a) where a primary source, which models a base station (*BTS*) or a generic wireless transmitter located at  $\mathbf{r}_{TX} = (r_{TX}, \theta_{TX}, \varphi_{TX})$ , illuminates a passive *EMS* in the origin of the *EMS* local coordinate system  $(x, y, z)$  with an incident time-harmonic field having electric/magnetic component  $\mathbf{F}_{inc}^o(\mathbf{r})$  ( $o \in \{e, h\}$ )<sup>(2)</sup>.

According to the *GSTC* formulation [5][17][19], the electric and the magnetic surface currents induced on the aperture  $\Omega$  of the *EMS* are given by

$$\mathbf{J}^e(\mathbf{r}) = j\omega\mathbf{P}_t^e(\mathbf{r}) - \hat{\nu} \times \nabla_t P_\nu^h(\mathbf{r}) \quad (1)$$

$$\mathbf{J}^h(\mathbf{r}) = j\omega\mu_0\mathbf{P}_t^h(\mathbf{r}) + \frac{1}{\varepsilon_0}\hat{\nu} \times \nabla_t P_\nu^e(\mathbf{r}) \quad (2)$$

where  $\hat{\nu}$  is the normal to the *EMS* surface,  $\nabla_t$  is the transverse gradient operator,  $\varepsilon_0$  and  $\mu_0$  are the free-space electric permittivity and magnetic permeability, respectively. Moreover,  $\mathbf{P}^o(\mathbf{r})$  ( $o \in \{e, h\}$ ) is the electric/magnetic polarization surface density,  $P_\nu^o(\mathbf{r})$  and  $P_t^o(\mathbf{r})$  being the normal component [ $P_\nu^o(\mathbf{r}) \triangleq \mathbf{P}^o(\mathbf{r}) \cdot \hat{\nu}$ ] and the transversal one [ $P_t^o(\mathbf{r}) \triangleq \mathbf{P}^o(\mathbf{r}) - P_\nu^o(\mathbf{r})\hat{\nu}$ ], respectively, that assumes the following expression [5][17][19]

$$\begin{aligned} \mathbf{P}^e(\mathbf{r}) &\approx \sum_{m=1}^M \sum_{n=1}^N \left[ \varepsilon_0 \overline{\overline{\psi}}^e(\mathbf{g}_{mn}) \cdot \mathbf{F}_{mn}^e \right]_{avg} \Upsilon_{mn}(\mathbf{r}) \\ \mathbf{P}^h(\mathbf{r}) &\approx \sum_{m=1}^M \sum_{n=1}^N \left[ \overline{\overline{\psi}}^h(\mathbf{g}_{mn}) \cdot \mathbf{F}_{mn}^h \right]_{avg} \Upsilon_{mn}(\mathbf{r}) \end{aligned} \quad (3)$$

for sufficiently symmetric unit cells of the *EMS* that consists of  $M \times N$  meta-atoms distributed

---

<sup>(2)</sup>For notation simplicity, the time-dependence term  $\exp(j\omega t)$  is omitted hereinafter.

on a uniform lattice with domains of area  $\Delta_x \times \Delta_y$ , centered at the positions  $\{\mathbf{r}_{mn} = (x_m, y_n) \in \Omega; m = 1, \dots, M; n = 1, \dots, N\}$ , and characterized by  $L$  geometrical/electrical descriptors,  $\mathbf{g}_{mn} \triangleq \{g_{mn}^l; l = 1, \dots, L\}$  ( $n = 1, \dots, N, m = 1, \dots, M$ ), that control the diagonal tensors of the electric/magnetic local surface susceptibilities [17]  $\overline{\overline{\psi}}^o(\mathbf{g}_{mn}) \triangleq \sum_{a=x,y,z} \psi_{aa}(\mathbf{g}_{mn}) \widehat{\mathbf{a}}\widehat{\mathbf{a}}$  ( $o \in \{e, h\}$ ). Moreover,  $\Upsilon_{mn}$  [ $\Upsilon_{mn}(\mathbf{r}) \triangleq \{1 \text{ if } \mathbf{r} \in \Omega_{mn}, 0 \text{ if } \mathbf{r} \notin \Omega_{mn}\}$ ] is the  $(m, n)$ -th ( $m = 1, \dots, M; n = 1, \dots, N$ ) basis function defined on the support  $\Omega_{mn}$  [ $\Omega_{mn} \triangleq \{x_m - \frac{\Delta_x}{2} \leq x \leq x_m + \frac{\Delta_x}{2}; y_n - \frac{\Delta_y}{2} \leq y \leq y_n + \frac{\Delta_y}{2}\}$ ;  $\Omega = \bigcup_{n=1}^N \bigcup_{m=1}^M \Omega_{mn}$ ], while  $\mathbf{F}_{mn}^o|_{avg}$  is the corresponding surface averaged field given by [5][17][19]

$$\mathbf{F}_{mn}^o|_{avg} = \frac{\int_{x_m - \frac{\Delta_x}{2}}^{x_m + \frac{\Delta_x}{2}} \int_{y_n - \frac{\Delta_y}{2}}^{y_n + \frac{\Delta_y}{2}} [\mathbf{F}_{inc}^o(\mathbf{r}) + \overline{\overline{\Gamma}}_{mn} \cdot \mathbf{F}_{inc}^o(\mathbf{r})] dx dy}{2 \times \Delta_x \times \Delta_y}, \quad (4)$$

$$\overline{\overline{\Gamma}}_{mn} \triangleq \begin{bmatrix} \Gamma_{\perp\perp}(\mathbf{g}_{mn}) & \Gamma_{\parallel\perp}(\mathbf{g}_{mn}) \\ \Gamma_{\perp\parallel}(\mathbf{g}_{mn}) & \Gamma_{\parallel\parallel}(\mathbf{g}_{mn}) \end{bmatrix} \text{ being the local reflection tensor.}$$

According to the Love's equivalence principle [15], the field reflected by an *EMS* in an arbitrary location  $\mathbf{r}$ ,  $\{\mathbf{F}_{ref}^o(\mathbf{r}), o \in \{e, h\}\}$ , turns out to be equal to that radiated in free-space by the equivalent current  $\mathbf{J}^o(\mathbf{r})$  ( $o \in \{e, h\}$ ) in (1)-(2). Moreover,  $\mathbf{F}_{ref}^o(\mathbf{r})$  ( $o \in \{e, h\}$ ) can be expressed in terms of the auxiliary electric

$$\mathbf{A}^e(\mathbf{r}) = \frac{\mu_0}{4\pi} \int_{\Omega} \mathbf{J}^e(\mathbf{r}') \frac{\exp(-jk_0 |\mathbf{r} - \mathbf{r}'|)}{|\mathbf{r} - \mathbf{r}'|} d\mathbf{r}' \quad (5)$$

and magnetic

$$\mathbf{A}^h(\mathbf{r}) = \frac{\varepsilon_0}{4\pi} \int_{\Omega} \mathbf{J}^h(\mathbf{r}') \frac{\exp(-jk_0 |\mathbf{r} - \mathbf{r}'|)}{|\mathbf{r} - \mathbf{r}'|} d\mathbf{r}' \quad (6)$$

vector potentials as follows [15]

$$\mathbf{F}_{ref}^e(\mathbf{r}) = -j\omega \mathbf{A}^e(\mathbf{r}) - \frac{j}{\omega\mu_0\varepsilon_0} \nabla(\nabla \cdot \mathbf{A}^e(\mathbf{r})) - \frac{1}{\varepsilon_0} \nabla \times \mathbf{A}^h(\mathbf{r}) \quad (7)$$

$$\mathbf{F}_{ref}^h(\mathbf{r}) = -\frac{1}{j\omega\mu_0} \nabla \times \mathbf{F}_{ref}^e(\mathbf{r}), \quad (8)$$

$k_0 \triangleq \omega\sqrt{\varepsilon_0\mu_0}$  being the free-space wavenumber. Therefore, field distribution  $\mathbf{F}_{ref}^o(\mathbf{r})$  ( $o \in \{e, h\}$ ) may be computed by substituting (1)-(2) in (5) and (6), and numerically integrating the

arising  $\{\mathbf{A}^o(\mathbf{r}); o \in \{e, h\}\}$  expressions to be then used in (7). However, such an approach is here avoided since it is numerically cumbersome and it is difficult to derive simple guidelines for the *EMS* synthesis. Otherwise, the prediction of  $\mathbf{F}_{ref}^o$  is carried out as detailed in the following. Let us start from the observation that the exponential term in (5) and (6) can be approximated as [15]

$$\frac{\exp(-jk_0 |\mathbf{r} - \mathbf{r}'|)}{|\mathbf{r} - \mathbf{r}'|} \approx \frac{\exp(-jk_0 r) \exp(jk_0 r' \cos \chi) \exp\left(-jk_0 \frac{(r' \sin \chi)^2}{2r}\right)}{r}, \quad (9)$$

$\chi$  being the angle between  $\mathbf{r}$  and  $\mathbf{r}'$ , while  $r \triangleq |\mathbf{r}|$  and  $r' \triangleq |\mathbf{r}'|$ , when the “*Fresnel condition*” holds true

$$\begin{cases} r \geq 10D \\ r \geq 0.62\sqrt{\frac{D^3}{\lambda_0}} \end{cases}. \quad (10)$$

In (10),  $\lambda_0 = \frac{2\pi}{k_0}$  is the free-space wavelength and  $D$  is the diameter of the smallest sphere containing the *EMS* surface current  $\mathbf{J}^o(\mathbf{r})$  ( $o \in \{e, h\}$ ), that is

$$D \triangleq \sqrt{(M \times \Delta_x)^2 + (N \times \Delta_y)^2}. \quad (11)$$

It is worth pointing out that (10) defines the *R-NF region*, which contains, as a sub-case, the *FF* one [15]. Therefore, the proposed formulation is expected to hold true for both *R-NF* and *FF* regions. Further well-known approximations of (9) can be derived for wider  $r$  values (i.e., if  $r \geq \frac{2D^2}{\lambda}$  [15]), but they will be neglected owing to the objective of deriving a generalized mathematical model for the *EM* behavior of *EMS*s used in wireless communications.

By substituting (9) in (5), one obtains that

$$\mathbf{A}^e(\mathbf{r}) \approx \frac{\mu_0}{4\pi} \frac{\exp(-jk_0 r)}{r} \int_{\Omega} \mathbf{J}^e(\mathbf{r}') \exp(jk_0 r' \cos \chi) \exp\left(-jk_0 \frac{(r' \sin \chi)^2}{2r}\right) d\mathbf{r}' \quad (12)$$

and a similar expression for  $\mathbf{A}^h(\mathbf{r})$  by simply replacing  $\mathbf{J}^e(\mathbf{r}') \leftarrow \mathbf{J}^h(\mathbf{r}')$  and  $\mu_0 \leftarrow \varepsilon_0$ .

Successively, subject to the condition

$$r \geq 10\lambda \quad (13)$$

and using (12) in (7), it can be proved (see “Appendix A.1”) that

$$\mathbf{F}_{ref}^e(\mathbf{r}) \approx -\frac{j \exp(-jk_0 r)}{2\lambda_0 r} \left\{ [\eta_0 S_\theta^e(\mathbf{r}) + S_\varphi^h(\mathbf{r})] \hat{\boldsymbol{\theta}} + [\eta_0 S_\varphi^e(\mathbf{r}) - S_\theta^h(\mathbf{r})] \hat{\boldsymbol{\varphi}} \right\} \quad (14)$$

where

$$\mathbf{S}^o(\mathbf{r}) \triangleq \int_{\Omega} \mathbf{J}^o(\mathbf{r}') \exp(jk_0 r' \cos \chi) \exp\left(-jk_0 \frac{(r' \sin \chi)^2}{2r}\right) d\mathbf{r}' \quad (15)$$

is the generalization of the radiation vector that here, unlike the traditional *FF* radiation theory [15], depends on  $r$ , as well.

The expression (14) allows one to derive in algebraic-form the field reflected by an arbitrary *EMS* in any scenario starting from the induced electric and magnetic surface currents (1)-(2) once (15) has been numerically evaluated. Towards this end, the surface current distribution  $\mathbf{J}^o$  ( $o \in \{e, h\}$ ) is firstly discretized by using the same set of basis functions in (3)

$$\mathbf{J}^o(\mathbf{r}) = \sum_{a=x,y} \sum_{m=1}^M \sum_{n=1}^N (J_a^o)_{mn} \Upsilon_{mn}(\mathbf{r}) \hat{\mathbf{a}} \quad (16)$$

where  $(J_a^o)_{mn}$  is the coefficient of the  $a$ -th ( $a \in \{x, y\}$ ) component of the  $o$ -th surface ( $o \in \{e, h\}$ ) current in the  $(m, n)$ -th ( $m = 1, \dots, M; n = 1, \dots, N$ ) *EMS* sub-domain.

By replacing (16) in (15) and reordering the linear operators, it turns out that

$$\mathbf{S}^o(\mathbf{r}) \triangleq \sum_{a=x,y} \hat{\mathbf{a}} \left[ \sum_{m=1}^M \sum_{n=1}^N (J_a^o)_{mn} \gamma_{mn}(\mathbf{r}) \right] \quad (17)$$

where

$$\gamma_{mn}(\mathbf{r}) \triangleq \int_{x_m - \frac{\Delta x}{2}}^{x_m + \frac{\Delta x}{2}} \int_{y_n - \frac{\Delta y}{2}}^{y_n + \frac{\Delta y}{2}} \exp(jk_0 r' \cos \chi) \exp\left(-jk_0 \frac{(r' \sin \chi)^2}{2r}\right) dx' dy'. \quad (18)$$

The discretized expression of the radiation vector in (17) is then decomposed in its spherical components

$$\begin{aligned} S_\theta^o(\mathbf{r}) &\triangleq \sum_{m=1}^M \sum_{n=1}^N \left\{ [(J_x^o)_{mn} \cos \theta \cos \varphi + (J_y^o)_{mn} \cos \theta \sin \varphi] \gamma_{mn}(\mathbf{r}) \right\} \\ S_\varphi^o(\mathbf{r}) &\triangleq \sum_{m=1}^M \sum_{n=1}^N \left\{ [-(J_x^o)_{mn} \sin \varphi + (J_y^o)_{mn} \cos \varphi] \gamma_{mn}(\mathbf{r}) \right\} \end{aligned} \quad (19)$$

to be substituted in (14) for yielding through simple manipulations (see ‘‘Appendix A.2’’) the final closed-form of the electric field reflected by an *EMS*



$$\begin{aligned}
\mathbf{F}_{ref}^e(\mathbf{r}) \approx & -\frac{j \exp(-jk_0 r)}{2\lambda_0 r} \sum_{m=1}^M \sum_{n=1}^N \text{sinc} \left[ \frac{\pi \Delta_x}{\lambda_0} u \right] \text{sinc} \left[ \frac{\pi \Delta_y}{\lambda_0} v \right] \Delta_x \Delta_y \\
& \exp \left\{ j \frac{\pi}{\lambda_0} \left( 2(x_m u + y_n v) - \frac{1}{r} [(x_m w)^2 + (y_n w)^2 + (x_m v - y_n u)^2] \right) \right\} \\
& \left\{ \left[ \eta_0 \cos \theta \cos \varphi (J_x^e)_{mn} + \eta_0 \cos \theta \sin \varphi (J_y^e)_{mn} - \sin \varphi (J_x^h)_{mn} + \cos \varphi (J_y^h)_{mn} \right] \hat{\boldsymbol{\theta}} + \right. \\
& \left. + \left[ -\eta_0 \sin \varphi (J_x^e)_{mn} + \eta_0 \cos \varphi (J_y^e)_{mn} + \cos \theta \cos \varphi (J_x^h)_{mn} + \cos \theta \sin \varphi (J_y^h)_{mn} \right] \hat{\boldsymbol{\varphi}} \right\}. \tag{20}
\end{aligned}$$

where  $u \triangleq \sin \theta \cos \varphi$ ,  $v \triangleq \sin \theta \sin \varphi$ , and  $w \triangleq \cos \theta$  [15].

Such an expression (20) allows one to faithfully predict the *EMS* reflection as a simple double summation of the surface currents when the conditions (10) and (13) are fulfilled. Moreover, it can be easily proved that (20) reduces to the relation for the *FF* approximation [5] when  $r \rightarrow \infty$ , since

$$\gamma_{mn}(r, u, v, w) \rightarrow \exp \left[ j \frac{2\pi}{\lambda_0} (x_m u + y_n v) \right] \Delta_x \Delta_y \text{sinc} \left[ \frac{\pi \Delta_x}{\lambda_0} u \right] \text{sinc} \left[ \frac{\pi \Delta_y}{\lambda_0} v \right]. \tag{21}$$

On the other hand, it must be noted that (20) does not hold true in the *reactive* near field region [15]. While this latter scenario does not generally arise in wireless communications, the prediction of the corresponding field distribution,  $\mathbf{F}_{ref}^e(\mathbf{r})$ , can be numerically performed by using (7) along with the discretized versions of (5) and (6), but without benefiting of simple algebraic closed-form expressions as in the other regimes (20).

### 3 Unified *EMS*-Synthesis Method

According to the guidelines in [5][17][19] for wireless communications, the design of an *EMS* able to maximize the power received by a terminal located at  $\mathbf{r} = \mathbf{r}_{RX}$  [ $\mathbf{r}_{RX} \triangleq (r_{RX}, \theta_{RX}, \varphi_{RX})$ ] can be formulated as that of finding the *EMS* descriptors such that the received power [15]

$$\Psi_{RX} = \frac{\lambda_0^2 G_{RX}^{\max}}{8\pi\eta_0} |\mathbf{F}_{ref}^e(\mathbf{r}_{RX})|^2 \tag{22}$$

is maximized,  $G_{RX}^{\max}$  being the maximum gain of the receiver, which is assumed to be aligned and perfectly matched in polarization. This problem is here addressed by first (a) synthesizing the ideal surface currents,  $\tilde{\mathbf{J}}^o(\mathbf{r})$  ( $o \in \{e, h\}$ ), that maximize the incident power at the receiver

$$\left\{ \tilde{\mathbf{J}}^o(\mathbf{r}); o \in \{e, h\} \right\} = \arg \left\{ \max \left[ \left| \mathbf{F}_{ref}^e(\mathbf{r}_{RX}) \right|^2 \right] \right\}, \quad (23)$$

and subsequently by (b) identifying the optimal setting of the *EMS* descriptors

$$\mathcal{G}^{opt} \triangleq \left\{ \mathbf{g}_{mn}^{opt}; m = 1, \dots, M, n = 1, \dots, N \right\} \quad (24)$$

that support the surface currents,  $\{\mathbf{J}^o(\mathbf{r}); o \in \{e, h\}\}$ , whose *phase* distributions within the *EMS* aperture  $\Omega$  closely match the ideal ones by minimizing the phase mismatch cost function

$$\Phi(\mathcal{G}) = \sum_{o=e,h} \sum_{a=x,y} \left[ \int_{\Omega} |\Delta J_a^o(\mathbf{r}; \mathcal{G})|^2 d\mathbf{r} \right] \quad (25)$$

where  $\Delta J_a^o(\mathbf{r}; \mathcal{G}) \triangleq \arg \left[ \tilde{J}_a^o(\mathbf{r}) \right] - \arg \left[ J_a^o(\mathbf{r}; \mathcal{G}) \right]$  (i.e.,  $\mathcal{G}^{opt} = \arg \{ \min_{\mathcal{G}} \Phi(\mathcal{G}) \}$ ).

As a matter of fact, owing to the passive nature of an *EMS*, the optimization of its micro-scale structure does not actually allow a fine control of the current magnitude,  $|\mathbf{J}^o(\mathbf{r})|$  ( $o \in \{e, h\}$ ). More specifically, it turns out that a suitable arrangement of the *EMS* meta-atoms carefully shapes only the phase distribution of the surface currents, while the magnitudes are inherited by the field radiated from the primary source on the *EMS* aperture [5][17][19].

Let us now detail the Step (a) concerned with the synthesis of  $\tilde{\mathbf{J}}^o(\mathbf{r})$  ( $o \in \{e, h\}$ ) (23). An approach different from the usual *FF*-focusing *EMS* strategy [5][19] is required since the expression of  $\left| \mathbf{F}_{ref}^e(\mathbf{r}_{RX}) \right|^2$  in (22) to be maximized is now (20), which extends and generalizes the most commonly adopted *FF*-approximated one [5][19]. Towards this end, the well-known phase-conjugation technique [21] is used so that, by cancelling the exponential terms in (20), all current terms are added *in-phase* at the focusing point. Accordingly, it turns out that if

$$\arg \left( \tilde{J}_a^o \right)_{mn} = - \arg \left[ \gamma_{mn}(r_{RX}, u_{RX}, v_{RX}, w_{RX}) \right] \quad (26)$$

( $o \in \{e, h\}; a \in \{x, y\}$ ) where  $u_{RX} = \sin \theta_{RX} \cos \varphi_{RX}$ ,  $v_{RX} = \sin \theta_{RX} \sin \varphi_{RX}$  and  $w_{RX} = \cos \theta_{RX}$ , then the addends of the summation in (20) can be elided. Thus, by substituting (40) in (26), the following closed-form rule for the synthesis of the optimal phase distribution of the *EMS* currents components ( $o \in \{e, h\}; a \in \{x, y\}$ ) is derived

$$\arg \left( \tilde{J}_a^o \right)_{mn} = \frac{\pi}{\lambda_0 r_{RX}} \left( (x_m w_{RX})^2 + (y_n w_{RX})^2 + (x_m v_{RX} - y_n u_{RX})^2 \right) + \quad (27)$$

$$- \frac{2\pi}{\lambda_0} (x_m u_{RX} + y_n v_{RX}).$$

It is worth remarking that (27) allows one to analytically synthesize the surface currents without local/global optimization processes. Moreover, it reduces to the well-known *FF* steering when  $r_{RX} \rightarrow \infty$  (i.e.,  $\arg \left( \tilde{J}_a^o \right)_{mn} \rightarrow -\frac{2\pi}{\lambda_0} (x_m u_{RX} + y_n v_{RX})$ ,  $o \in \{e, h\}$ ,  $a \in \{x, y\}$ ), as theoretically expected.

Finally, the power pattern in the focusing point  $\mathbf{r} = \mathbf{r}_{RX}$  is determined by substituting (27) in (20)

$$\left| \mathbf{F}_{ref}^e(\mathbf{r}_{RX}) \right|^2 \approx \left( \frac{1}{2\lambda_0 r} \right)^2 \sum_{m=1}^M \sum_{n=1}^N \left\{ \left[ \eta_0 \cos \theta \cos \varphi \left| (J_x^e)_{mn} \right| + \eta_0 \cos \theta \sin \varphi \left| (J_y^e)_{mn} \right| - \sin \varphi \left| (J_x^h)_{mn} \right| + \cos \varphi \left| (J_y^h)_{mn} \right| \right]^2 + \right. \\ \left. + \left[ -\eta_0 \sin \varphi \left| (J_x^e)_{mn} \right| + \eta_0 \cos \varphi \left| (J_y^e)_{mn} \right| + \cos \theta \cos \varphi \left| (J_x^h)_{mn} \right| + \cos \theta \sin \varphi \left| (J_y^h)_{mn} \right| \right]^2 \right\}. \quad (28)$$

As for the ‘‘Step (b)’’, the *System-by-Design (SbD)* [20] implementation, proposed in [5][19], is adopted and summarized in the following. A succession of  $I$  *SbD* iterations ( $i = 1, \dots, I$ ) is performed [20] to find  $\mathcal{G}^{opt}$ . At each  $i$ -th ( $i = 1, \dots, I$ ) iteration,  $B$  guess *EMS* layouts,  $\{\mathcal{G}_b^{(i)} \triangleq \{\mathbf{g}_{mn}\}_b^{(i)}; m = 1, \dots, M, n = 1, \dots, N\}; b = 1, \dots, B\}$ , are generated by (i) the *solution-space-exploration* block, which is implemented according to the *particle swarm* evolutionary algorithm [20]. The corresponding  $B$  diagonal tensors of the local surface susceptibilities,  $\{\overline{\psi}^o \left( \mathbf{g}_{mn} \right)_b^{(i)}\}$  ( $o \in \{e, h\}; b = 1, \dots, B\}$ , are then selected in (ii) the *local susceptibility look-up table*, whose entries have been offline-computed with the full-wave Ansys HFSS [18] commercial SW, and inputted into (iii) the *electric/magnetic surface current computation* block that implements (3) to compute the polarization surface densities,  $\{\mathbf{P}^o \left( \mathbf{r}; \mathcal{G}_b^{(i)} \right)\}$  ( $o \in \{e, h\}; b = 1, \dots, B\}$ , to yield  $\{\mathbf{J}^o \left( \mathbf{r}; \mathcal{G}_b^{(i)} \right)\}$  ( $o \in \{e, h\}; b = 1, \dots, B\}$  through (1)-(2). The surface currents are then provided to (iv) the *physical linkage* block that computes the corresponding cost function values (25),  $\{\Phi \left( \mathcal{G}_b^{(i)} \right)\}; b = 1, \dots, B\}$ . The iterative loop of (i)-(iv) is repeated until the maximum number of iterations is reached,  $i = I$ , or alternative convergence conditions (e.g., the stationarity of the cost function value [20]) are met. The final layout of the *EMS* is then defined as  $\mathcal{G}^{opt} = \arg \left\{ \min_{i=1, \dots, I; b=1, \dots, B} \left[ \Phi \left( \mathcal{G}_b^{(i)} \right) \right] \right\}$ .

## 4 Numerical Validation and Performance Assessment

The objective of this Section is twofold. On the one hand (Sect. 4.1), it is aimed at validating the “Generalized *EMS*-Analysis” presented in Sect. 2 for predicting the *EM* field reflected by an *EMS* in wireless communication scenarios. On the other hand (Sect. 4.2), it is devoted to assess the effectiveness and the efficiency of the arising “*Unified EMS-Synthesis Method* “ (*USM*) (Sect. 3) with respect to the state-of-the-art *FF*-oriented method [5][19] (*FFM*) by considering full-wave simulations as reference ground truth.

Towards this end, the benchmark *SEE* scenario consists of a source operating at  $f = 17.5$  [GHz] and equipped with a linearly-polarized pyramidal horn antenna [Fig. 1(d)] that illuminates the *EMS* from  $(\theta_{TX}, \varphi_{TX}) = (30, 180)$  [deg]. To avoid any bias related to the exploitation of advanced/complex *EMS* unit cells, a canonical square-shaped patch of side  $\Delta l$  (i.e.,  $\Delta l_x = \Delta l_y = \Delta l$ ) with no via holes [Fig. 1(c)] has been chosen as elementary *EMS* meta-atom [ $\rightarrow L = 1 \Rightarrow g_{mn} \triangleq (\Delta l)_{mn}$  ( $n = 1, \dots, N, m = 1, \dots, M$ )]. This latter has been modeled in *HFSS* by considering a single-layer Rogers *RO4350* substrate with thickness  $\tau = 7.62 \times 10^{-4}$  [m] and a half-wavelength (i.e.,  $\Delta_x = \Delta_y = \Delta = 8.565 \times 10^{-3}$  [m]) uniform lattice. Moreover, the calibration parameters of the *SbD*-based synthesis process have been set according to the guidelines in [5][19]:  $B = 10$  and  $I = 10^4$ .

### 4.1 *EMS*-Analysis Validation

In order to assess the reliability and the accuracy of the prediction method in Sect. 2, comparisons with full-wave simulations, carried out with *Ansys HFSS* [18], have been considered and the results from the analysis of three representative *EMS*s<sup>(3)</sup> will be illustrated hereinafter.

The first test case deals with an *EMS* [Fig. 3(a)] defined on a lattice of  $M \times N = 48 \times 48$  domains (i.e., a square panel of side  $\mathcal{L} \approx 0.41$  [m]), composed by uniform square meta-atoms of side  $\Delta l = 5.0 \times 10^{-3}$  [m], and illuminated by a  $G_{TX}^{\max} = 20.4$  [dBi] horn antenna (see Tab. I - second column), which is located a distance of  $r_{TX} = 50$  [m] from the *EMS* and fed by a  $\Xi_{TX} = 20$  [dBm]-power transmitter, that generates on the *EMS* aperture  $\Omega$  an incident  $y$ -

<sup>(3)</sup>The *EMS* apertures have been chosen to keep reasonable/feasible the time/memory requirements for their *HFSS* simulation on a standard workstation (e.g., a workstation equipped with 512 GB of RAM and a 32-core 3.5 GHz CPU).

polarized electric field whose magnitude and phase distributions are shown in Fig. 2(a) and Fig. 2(b), respectively. The *EM* field reflected by the *EMS* has been predicted with the generalized theory (20) and the traditional *FF* radiation theory [15], while it has been *HFSS*-computed by modeling the finite structure of the *EMS* and the transmitting horn antennas with the *Finite Element Boundary Integral (FEBI)* approach.

Figure 4 shows the co-polar field magnitude,  $|F_{ref,\varphi}^e(\mathbf{r})|$ , in the two planes  $\Theta_{NF}$  and  $\Theta_{FF}$  of Fig. 1(b) along the angular direction  $\theta = 30$  [deg]. More specifically, the former is located in the *R-NF* region of the *EMS*,  $r = 6$  [m] ( $\mathbf{r} \in \Theta_{NF}$ ,  $r > r_{NF}$ ,  $r_{NF} = 5.82$  [m] since  $r_{NF} \triangleq \min \left\{ 10 D; 10 \lambda; 0.62 \sqrt{\frac{D^3}{\lambda}} \right\}$ ) far from the *EMS* aperture  $\Omega$ . The other is  $r = 40$  [m] from  $\Omega$  in the *EMS FF* region ( $\mathbf{r} \in \Theta_{FF}$ ,  $r > r_{FF}$ ,  $r_{FF} = 39.50$  [m],  $r_{FF}$  being  $r_{FF} \triangleq \min \left\{ 10 D; 10 \lambda; \frac{2 \times D^2}{\lambda} \right\}$ ). As expected, while both predictions are very close to the actual/*HFSS*-computed *EM* distribution in the *FF* plane  $\Theta_{FF}$  [Figs. 4(d)-4(e) vs. Fig. 4(f)] since (20) reduces to the relation for the *FF* approximation [5] when  $r \rightarrow \infty$ , the generalized approach gives a better estimate of the field reflected by the *EMS* in the *R-NF* plane  $\Theta_{NF}$  [Fig. 4(b) vs. Figs. 4(c)] as highlighted by the corresponding map of the prediction error, which is defined as

$$\Delta F_{ref,\varphi}^e(\mathbf{r}) \triangleq \frac{\left| F_{ref,\varphi}^e(\mathbf{r}) \Big|_{Predicted} - F_{ref,\varphi}^e(\mathbf{r}) \Big|_{HFSS-Computed} \right|^2}{\max_{\mathbf{r} \in \Theta} \left| F_{ref,\varphi}^e(\mathbf{r}) \Big|_{HFSS-Computed} \right|^2}, \quad (29)$$

in Fig. 5(b), as compared to that in Fig. 5(a) for the traditional *FF* theory [15]. It is worth pointing out that the marginal deviations from the *HFSS* values, as shown in Fig. 5(b), are caused by the unavoidable approximations due to the discretization of the surface currents with a  $\Delta_x \times \Delta_y$  step (16) as well as by the truncation/edge scattering effects of the finite *EMS* at hand.

The other two test cases refer to the non-uniform *EMS*s shown in Figs. 3(b)-3(c) arranged on a uniform lattice of  $M \times N = 84 \times 84$  (i.e.,  $\mathcal{L} = 0.72$  [m])  $\Delta$ -sized domains. By keeping the same setup of the previous experiment and performing the same analysis, it turns out that similar conclusions on the reliability and the accuracy of the generalized approach can still be drawn. Indeed, the maps of  $\Delta F_{ref,\varphi}^e(\mathbf{r})$  in  $\Theta_{NF}$  ( $r = 10.5$  [m] and  $\theta = 10$  [deg] being  $r_{NF} = 10.18$

[m]) significantly differ [Fig. 6(a) vs. Fig. 6(b) and Fig. 6(c) vs. Fig. 6(d)], while those in  $\Theta_{FF}$  ( $r = 121$  [m] and  $\theta = 10$  [deg] being  $r_{FF} = 120.96$  [m]) look almost equal [Fig. 7(a) vs. Fig. 7(b) and Fig. 7(c) vs. Fig. 7(d)].

As for the computational efficiency of the proposed approach, a proof is that an *EM* prediction of the field reflected by an  $M \times N = 84 \times 84$  (i.e.,  $\mathcal{L} = 0.72$  [m]) *EMS* with the generalized formulation is yielded in  $\Delta t^{Generalized Theory} \approx 2.1$  [s] with a non-optimized Matlab implementation, while the corresponding full-wave computation needs  $\Delta t^{HFSS} \approx 2.6 \times 10^6$  [s].

## 4.2 EMS-Synthesis Assessment

The first test case of the numerical assessment of the synthesis method in Sect. 3 is concerned with the design of a  $M \times N = 120 \times 120$  *EMS* ( $\rightarrow \mathcal{L} \approx 1.029$  [m]) illuminated by a source, located at a distance of  $r_{TX} = 50$  [m] from  $\Omega$  and modeled with a  $G_{TX}^{\max} = 13.7$  [dBi] horn antenna (see Tab. I - first column) that generates on the *EMS* an incident *y*-polarized electric field whose magnitude and phase distributions are shown in Fig. 2(c) and Fig. 2(d), respectively. The *EMS* is required to establish a wireless link with a terminal located  $r_{RX} = 15$  [m] far from the *EMS* along the anomalous/non-Snell angular direction  $(\theta_{RX}, \varphi_{RX}) = (10, 0)$  [deg] where a horn antenna of the same type of the transmitting one has been used as receiver<sup>(4)</sup>. Since both (10) and (13) conditions are fulfilled and the *R-NF* region of the *EMS* at hand starts at  $r > r_{NF} = 14.54$  [m], while the *FF* one initiates at  $r > r_{FF} = \frac{2D^2}{\lambda_0} = 246.86$  [m], the theoretical approach formulated in Sect. 2 holds true and the arising *EMS* synthesis method (Sect. 3) can be reliably applied. Accordingly, the reference phase distribution of the surface currents on the *EMS*,  $\arg\left(\tilde{J}_a^o\right)_{mn}$ ,  $o \in \{e, h\}$ ,  $a \in \{x, y\}$ , is firstly [Step (a)] computed with (27). As expected ( $r \approx r_{NF}$ ), the arising phase profile [Fig. 8(b) -  $o = e$ ,  $a = x$ ] significantly differs from that obtained with a standard *FF* focusing process [17] [Fig. 8(a)]. The subsequent Step (b) is then aimed at determining the *EMS* descriptors,  $\mathcal{G}^{opt} \triangleq \left\{ g_{mn} \triangleq (\Delta l)_{mn}; m = 1, \dots, M, n = 1, \dots, N \right\}$ , that allow the wave incident on the *EMS* (Fig. 2) to induce a surface current,  $\mathbf{J}^o$ , matching the reference one,  $\tilde{\mathbf{J}}^o$ , by minimizing the phase mismatch cost function  $\Phi(\mathcal{G})$  (25). Owing to the simplicity of the meta-atom at hand, the

<sup>(4)</sup>For the sake of simplicity, both transmitter and receiver have been modeled with the same elementary radiator. However, the *EMS* design process is independent on the receiving antenna.

synthesized phase profile [Fig. 8(d)] does not perfectly reproduce the reference one [Fig. 8(b)] in each unit cell location, but the overall behavior is complied with [Fig. 8(d) vs. Fig. 8(b)]. For the same reason, a similar mismatch can be also observed in the case of the *FF* design [Fig. 8(c) vs. Fig. 8(a)] as quantitatively confirmed by the values of the corresponding cumulative distribution function of the phase mismatch,  $|\Delta J_y^e(\mathbf{r}; \mathcal{G}^{opt})|$ , in Fig. 8(e). On the contrary, the *EMS* layouts synthesized in the Step (b) are not alike [Fig. 9(a) vs. Fig. 9(b)]. This implies that there are significant differences [Fig. 9(d) vs. Fig. 9(c)] in the magnitude of the dominant component of  $\mathbf{F}_{ref}^e(\mathbf{r})$  reflected in the receiver plane  $\Theta_{RX}$  [Fig. 1(b)]. As a matter of fact, the focusing of the field reflected by the *EMS* synthesized with the *USM* (Sect. 3) significantly improves and the received power  $\Psi_{RX}$  increases up to  $\Psi_{RX}^{USM} \approx -33.05$  [dBm] from the value of  $\Psi_{RX}^{FFM} \approx -41.34$  [dBm] yielded with the *FFM* despite the same  $\mathcal{L}$  and transmitting source. The second experiment of this section (Sect. 4.2) is then aimed at assessing the dependence of the *USM* performance on the receiver distance  $r_{RX}$  by keeping the same design setup of the first test case, but varying  $r_{RX}$ . Figure 10 shows that  $\Psi_{RX}^{USM} \geq \Psi_{RX}^{FFM}$  regardless of the distance of the receiver from the *EMS*. The power improvement guaranteed by the *USM*,  $\Delta\Psi_{RX}$  ( $\Delta\Psi_{RX} \triangleq \frac{\Psi_{RX}^{USM} - \Psi_{RX}^{FFM}}{\Psi_{RX}^{FFM}}$ ), reduces as  $r_{RX}$  increases (e.g.,  $\Delta\Psi_{RX}|_{r_{RX}=15\text{ m}} \approx 7.59$  [dB] vs.  $\Delta\Psi_{RX}|_{r_{RX}=50\text{ m}} \approx -7.63$  [dB] - Fig. 10). This is theoretically expected since both (20) and (26) reduce to their *FF* counterparts [5] when  $r \rightarrow \infty$  (i.e., *FF* conditions occur).

The effectiveness of the *USM* to deal with different *EMS* apertures is addressed next. Towards this end, the design process has been carried out by ranging the *EMS* size and the receiver distance in the range  $12 \times 12 \leq M \times N \leq 240 \times 240$  (i.e.,  $1.03 \times 10^{-1}$  [m]  $\leq \mathcal{L} \leq 2.057$  [m]) and  $30$  [m]  $\leq r_{RX} \leq 150$  [m], respectively. The results yielded by applying the *USM* and the *FFM* are summarized in Fig. 11 in terms of the power received by the terminal,  $\Psi_{RX}$ . By comparing the maps of  $\Psi_{RX}^{FFM}$  [Fig. 11(a)] and  $\Psi_{RX}^{USM}$  [Fig. 11(b)] in the domain  $(\mathcal{L}, r_{RX})$ , it turns out that the two approaches perform similarly when the receiver is in the *FF* of the *EMS* [i.e.,  $\Psi_{RX}^{USM} \approx \Psi_{RX}^{FFM} \rightarrow \Delta\Psi_{RX} \approx -20$  [dB] - Fig. 11(c)]. Otherwise, it is more and more convenient (i.e.,  $\Delta\Psi_{RX} \uparrow$ ) to use the *USM* as  $\mathcal{L} \uparrow$  and  $r_{RX} \downarrow$  [e.g.,  $r_{RX} < 40$  [m] and  $\mathcal{L} > 1.3$  [m] - Fig. 11(c)],  $\Delta\Psi_{RX} \approx 30$  [dB] being the maximum “gain” within the range of values of this parametric analysis [Fig. 11(c)].

For the sake of completeness, the synthesized *EMS* layouts [Figs. 12(a)-12(b)] and the corresponding distributions of the co-polar field magnitude in the receiver cut  $\Theta_{RX}$  at  $r_{RX} = 30$  [m] [Figs. 12(c)-12(d)] are reported for the case  $M \times N = 240 \times 240$  (i.e.,  $\mathcal{L} = 2.057$  [m]). The *USM* *EMS* significantly outperforms the *FFM* one in terms of focusing ability [Fig. 12(d) vs. Fig. 12(c)] with a relevant enhancement of the power received by the terminal ( $\Psi_{RX}^{USM} \approx -27.04$  [dBm] vs.  $\Psi_{RX}^{FFM} \approx -47.81$  [dBm]).

Next, the assessment of the *USM* potentialities is carried out with respect to the receiver location (Figs. 13-14). The behaviour of  $\Psi_{RX}$  as a function of  $r_{RX}$  for both anomalous ( $\theta_{RX} \neq 30$  [deg]) and Snell ( $\theta_{RX} = 30$  [deg]) directions of reflection ( $M \times N = 120 \times 120$ ,  $\mathcal{L} = 1.029$  [m]) indicates that once more the *USM* outperforms the traditional *FFM* independently on the  $\theta_{RX}$  value since always  $\Psi_{RX}^{USM} \geq \Psi_{RX}^{FFM}$  [Fig. 13(a)]. Moreover, as expected, the focusing improvement enabled by the *USM*,  $\Delta\Psi_{RX}$ , gets better and better as  $r_{RX} \downarrow$  and  $\theta_{RX} \downarrow$ . Furthermore, the values of  $\Psi_{RX}^{USM}$  increase as  $\theta_{RX} \rightarrow 0$  [deg] consistently with the fact that the gain of any radiating aperture is maximum along broadside. Differently, the behavior of  $\Psi_{RX}^{FFM}$  does not always comply with such a theoretical expectation because of the sub-optimal focusing performance of the *FFM* solution in the *R-NF* region [e.g.,  $\Psi_{RX}^{FFM}|_{\theta_{RX}=0[deg]} < \Psi_{RX}^{FFM}|_{\theta_{RX}=30[deg]}$  when  $r_{RX} < 18$  [m] - Fig. 13(a)].

Let us now analyze more in detail two representative scenarios of the test case at hand: ( $r_{RX} = 15$  [m];  $\theta_{RX} = \theta_{TX} = 30$  [deg]) and ( $r_{RX} = 15$  [m];  $\theta_{RX} = 50$  [deg]  $\rightarrow \theta_{RX} \neq \theta_{TX}$ ). The layouts synthesized with the *FFM* [Figs. 13(b)-13(c)] and the *USM* [Figs. 13(d)-13(e)] strongly differ when both Snell [Fig. 13(b) vs. Fig. 13(d)] or anomalous [Fig. 13(c) vs. Fig. 13(e)] reflections are forced. Analogously and consequently, the field profiles in  $\Theta_{RX}$  do not have evident similarities [Fig. 14(a) vs. Fig. 14(c) and Fig. 14(b) vs. Fig. 14(d)] by pointing out the superior performance of the *USM* in steering the reflected power towards the receiving terminal as quantitatively confirmed by the values of  $\Psi_{RX}$  plotted in Fig. 13(a) [i.e.,  $\Delta\Psi_{RX}|_{\theta_{RX}=30[deg]}^{r_{RX}=15[m]} \approx 5.03$  [dB] and  $\Delta\Psi_{RX}|_{\theta_{RX}=50[deg]}^{r_{RX}=15[m]} \approx 3.29$  [dB]).

Since the position of the illuminating source is not expected to affect the previous conclusions on the effectiveness of the *USM*, the *EMS* design process has been repeated by only changing the distance between the transmitter and the *EMS* within the range  $15$  [m]  $\leq r_{TX} \leq 100$  [m].



The plots of the power received by the terminal,  $\Psi_{RX}$ , versus  $r_{RX}$  in Fig. 15(a) confirm that always  $\Delta\Psi_{RX} \geq 0$  as well as that the improvement of the *USM* with respect to the *FFM* is almost independent on the distance of the *EMS* from the *BTS* (e.g.,  $\Delta\Psi_{RX}|_{r_{TX}=15[m]}^{r_{RX}=15[m]} \approx 7.56$  [dB] vs.  $\Delta\Psi_{RX}|_{r_{TX}=100[m]}^{r_{RX}=15[m]} \approx 7.59$  [dB]).

On the contrary, the position of the *BTS* impacts on the *EMS* layout as highlighted by the comparison of the unit-cell arrangements synthesized, when  $r_{TX} = 15$  [m] [Fig. 15(b) and Fig. 15(c)] or  $r_{TX} = 50$  [m] [Fig. 9(a) and Fig. 9(b)], with either the *FFM* [Fig. 15(b) vs. Fig. 9(a)] or the *USM* [Fig. 15(c) and Fig. 9(b)]. This is an obvious consequence of the two-step *EMS* synthesis strategy, since the incident field,  $\mathbf{F}_{inc}^o(\mathbf{r})$  ( $o \in \{e, h\}$ ), together with the micro-scale descriptors of the *EMS*,  $\mathcal{G}$ , control the surface currents induced on the *EMS* aperture (see Sect. 2) to focus the reflected wave towards the receiving terminal. On the other hand, the reader can notice that, analogously to the case in Fig. 9 [Fig. 9(d) vs. Fig. 9(c)], also here the *USM-EMS* better focus on the spot area than the *FFM* one [Fig. 15(e) vs. Fig. 15(d)].

To further analyze the dependence of the *USM* performance on the features of the primary source, the relatively low-gain horn (i.e.,  $G_{TX}^{\max} = 13.7$  [dBi] - Tab. I) located at  $r_{TX} = 50$  [m] from an  $M \times N = 120 \times 120$  (i.e.,  $\mathcal{L} = 1.029$  [m]) *EMS* has been then substituted with the higher gain horn (i.e.,  $G_{TX}^{\max} = 20.4$  [dBi] - Tab. I) to mimic a more directive transmitter. Moreover, the receiver has been still modeled with the same device of the transmitter, while its position has been varied as follows:  $15 \text{ [m]} \leq r_{RX} \leq 50 \text{ [m]}$  and  $\theta_{RX} \in \{10, 30, 50\}$  [deg]. The outcomes of this numerical study are summarized in Fig. 16 where the plots of  $\Psi_{RX}$  versus  $r_{RX}$  are shown. It turns out that there is an advantage of using the *USM* (i.e.,  $\Delta\Psi_{RX} \geq 0$ ) for any distance and whatever the angular position of the receiver both along the Snell direction (i.e.,  $\theta_{RX} = 30$  [deg]) or not (i.e.,  $\theta_{RX} \in \{10, 50\}$  [deg]). Moreover, as previously inferred, the improvement enabled by the *USM* is wider for reflection angles closer to the *EMS* broadside (e.g.,  $\Delta\Psi_{RX}|_{\theta_{RX}=10[deg]}^{r_{RX}=15[m]} \approx 7.59$  [dB] vs.  $\Delta\Psi_{RX}|_{\theta_{RX}=50[deg]}^{r_{RX}=15[m]} \approx 3.31$  [dB]). These results, which are fully consistent with those arising when using a less directive source [Fig. 16 vs. Fig. 13(a)], assess that the performance of the *USM*-based *EMS* synthesis are not affected by the illumination features.

The last experiment is devoted to prove that the analytic prediction of the received-power im-

provement enabled by the *USM* through (28) is accurate. Towards this end, the same benchmark setup of Fig. 16 has been used, while the synthesis of *EMS*s with  $M \times N = 84 \times 84$  unit cells (i.e.,  $\mathcal{L} = 0.72$  [m]) has been performed to steer the reflected waves along the angular direction  $\theta_{RX} = 10$  [deg] in different receiving spots within the interval  $15$  [m]  $\leq r_{RX} \leq 50$  [m]. Once the design process has been carried out with the *USM* and the *FFM*, the reflection performance of the arising layouts have been analytically predicted with (28) in (22),  $\Psi_{RX}^{Predicted}$ , or full-wave simulated in *Ansys HFSS* [18],  $\Psi_{RX}^{HFSS-Computed}$ . Both analytically-computed and full-wave simulated values of  $\Delta\Psi_{RX}$  are reported in Fig. 17. It turns out that the maximum deviation of the prediction from the actual value is below 0.5 [dB] (i.e.,  $0.4$  [dB]  $\leq \left| \Delta\Psi_{RX}^{HFSS-Computed} - \Delta\Psi_{RX}^{Predicted} \right| \leq 0.5$  [dB]) regardless of  $r_{RX}$ .

## 5 Conclusions

Within the *GSTC* theoretical framework and applying the classical theory of radiated fields, a mathematically rigorous derivation of a generalized expression of the *EM* field reflected by an *EMS* in the working regimes of interest for wireless communications has been presented to derive a unified method for the design of anomalous-reflecting and focusing *EMS*s.

Numerical results, along with comparisons with full-wave simulations, have been illustrated to assess the reliability and the accuracy of the proposed generalized method for the prediction of the *EM* behavior of *EMS*s as well as to prove the advantages of the arising unified strategy for the synthesis of *EMS*s over standard *FF*-based state-of-the-art design techniques.

From the numerical validation and performance assessment, the following outcomes can be drawn:

- the prediction of the *EM* field reflected by an *EMS* coming from the proposed generalized method (20) faithfully matches the full-wave computed one and it is obtained with a non-negligible time saving (i.e.,  $\frac{\Delta t^{Prediction}}{\Delta t^{HFSS}} > 10^6$ );
- the unified *EMS*-synthesis strategy always outperforms the state-of-the-art *FF*-based method regardless of the benchmark setup at hand (i.e.,  $\Psi_{RX}^{NF} \geq \Psi_{RX}^{FF}$ ), but the advantage of using the *USM* in terms of increment of the power received by the terminal (i.e.,  $\Delta\Psi_{RX}$ )

is greater when (a) the distance of the receiver from the *EMS* reduces ( $r_{RX} \downarrow$  being  $r_{RX} \geq r_{NF}$ ), (b) the *EMS* aperture,  $\Omega$ , widens ( $\mathcal{L} \uparrow$ ), and (c) the reflection angle,  $\theta_{RX}$ , becomes closer and closer to broadside ( $\theta_{RX} \downarrow$ ).

Future works, beyond the scope of the current manuscript, will be aimed at evaluating the unified *EMS* synthesis strategy when applied to the design of reconfigurable *EMS*s. Currently, the performance of *USM*-based *EMS*s with more complex unit cells are under investigation and they will be the topic of future publications.

## Appendix

### A.1 - Proof of (14)

By substituting (12) in (7) and using (15), it turns out that

$$\mathbf{F}_{ref}^e(\mathbf{r}) \approx -\frac{j\omega\mu_0}{4\pi} \frac{\exp(-jk_0r)}{r} \mathbf{S}^e(\mathbf{r}) - \frac{j}{4\pi\omega\epsilon_0} \nabla \left( \nabla \cdot \left[ \frac{\exp(-jk_0r)}{r} \mathbf{S}^e(\mathbf{r}) \right] \right) + \left(30\right) \\ - \frac{1}{4\pi} \nabla \times \left[ \frac{\exp(-jk_0r)}{r} \mathbf{S}^h(\mathbf{r}) \right].$$

Such an expression (30) can be simplified into (14) by rewriting the differential operators in spherical coordinates and neglecting the non-dominant radial terms (i.e.,  $(\frac{1}{r})^s$ ,  $s \geq 2$ ) as detailed in the following.

Let us first consider the explicit expression in spherical coordinates of the divergence term in the right-hand side of (30)

$$\nabla \cdot \left[ \frac{\exp(-jk_0r)}{r} \mathbf{S}^e(\mathbf{r}) \right] = \frac{1}{r^2} \frac{\partial}{\partial r} \left[ r \exp(-jk_0r) S_r^e(\mathbf{r}) \right] + \frac{\exp(-jk_0r)}{r^2 \sin \theta} \frac{\partial}{\partial \theta} \left[ \sin \theta S_\theta^e(\mathbf{r}) \right] + \left(31\right) \\ + \frac{\exp(-jk_0r)}{r^2 \sin \theta} \frac{\partial}{\partial \varphi} \left[ S_\varphi^e(\mathbf{r}) \right]$$

that, subject to the condition (13) and discarding the  $s = 2$ -th order radial dependence, simplifies as follows

$$\nabla \cdot \left[ \frac{\exp(-jk_0r)}{r} \mathbf{S}^e(\mathbf{r}) \right] \approx -jk_0 \frac{\exp(-jk_0r)}{r} S_r^e(\mathbf{r}). \left(32\right)$$

The gradient of (32) then turns out to be

$$\begin{aligned} \nabla \left( \nabla \cdot \left[ \frac{\exp(-jk_0 r)}{r} \mathbf{S}^e(\mathbf{r}) \right] \right) &\approx -jk_0 \frac{\partial}{\partial r} \left[ \frac{\exp(-jk_0 r)}{r} S_r^e(\mathbf{r}) \right] \hat{\mathbf{r}} - jk_0 \frac{\exp(-jk_0 r)}{r^2} \frac{\partial}{\partial \theta} [S_r^e(\mathbf{r})] \hat{\boldsymbol{\theta}} + \\ &\quad - jk_0 \frac{\exp(-jk_0 r)}{r^2 \sin \theta} \frac{\partial}{\partial \varphi} [S_r^e(\mathbf{r})] \hat{\boldsymbol{\varphi}} \end{aligned} \quad (33)$$

that, once again neglecting the non-dominant  $(\frac{1}{r})^2$  terms, reduces to

$$\nabla \left( \nabla \cdot \left[ \frac{\exp(-jk_0 r)}{r} \mathbf{S}^e(\mathbf{r}) \right] \right) \approx -k_0^2 \frac{\exp(-jk_0 r)}{r} S_r^e(\mathbf{r}) \hat{\mathbf{r}}. \quad (34)$$

As for the curl component in (30), the first-order truncated expression is

$$\nabla \times \left[ \frac{\exp(-jk_0 r)}{r} \mathbf{S}^h(\mathbf{r}) \right] \approx \frac{1}{r} \frac{\partial}{\partial r} \left[ -\exp(-jk_0 r) S_\varphi^h(\mathbf{r}) \hat{\boldsymbol{\theta}} + \exp(-jk_0 r) S_\theta^h(\mathbf{r}) \hat{\boldsymbol{\varphi}} \right] \quad (35)$$

that, after simple manipulation, becomes

$$\nabla \times \left[ \frac{\exp(-jk_0 r)}{r} \mathbf{S}^h(\mathbf{r}) \right] \approx -jk_0 \frac{\exp(-jk_0 r)}{r} \left[ S_\varphi^h(\mathbf{r}) \hat{\boldsymbol{\theta}} + S_\theta^h(\mathbf{r}) \hat{\boldsymbol{\varphi}} \right]. \quad (36)$$

Equation (14) is finally yielded by substituting (34) and (36) in (30).

## A.2 - Proof of (20)

By substituting (19) in (14), it turns out that

$$\begin{aligned} \mathbf{F}_{ref}^e(\mathbf{r}) &\approx -\frac{j \exp(-jk_0 r)}{2\lambda_0 r} \sum_{m=1}^M \sum_{n=1}^N \gamma_{mn}(\mathbf{r}) \times \\ &\left\{ \left[ \eta_0 \cos \theta \cos \varphi (J_x^e)_{mn} + \eta_0 \cos \theta \sin \varphi (J_y^e)_{mn} - \sin \varphi (J_x^h)_{mn} + \cos \varphi (J_y^h)_{mn} \right] \hat{\boldsymbol{\theta}} + \right. \\ &\left. + \left[ -\eta_0 \sin \varphi (J_x^e)_{mn} + \eta_0 \cos \varphi (J_y^e)_{mn} + \cos \theta \cos \varphi (J_x^h)_{mn} + \cos \theta \sin \varphi (J_y^h)_{mn} \right] \hat{\boldsymbol{\varphi}} \right\}. \end{aligned} \quad (37)$$

Let us then apply simple trigonometric operations to rewrite the arguments of the exponential of  $\gamma_{mn}$  (18) as follows

$$\begin{cases} r' \cos \chi = x'u + y'v \\ (r' \sin \chi)^2 = (x'w)^2 + (y'w)^2 + (x'v - y'u)^2 \end{cases}, \quad (38)$$

$u$ ,  $v$ , and  $w$  being the direction cosine coordinates [15].

Accordingly, the new expression of  $\gamma_{mn}(\mathbf{r})$  turns out to be

$$\gamma_{mn}(r, u, v, w) = \int_{x_m - \frac{\Delta_x}{2}}^{x_m + \frac{\Delta_x}{2}} \int_{y_n - \frac{\Delta_y}{2}}^{y_n + \frac{\Delta_y}{2}} \exp \left[ j \frac{2\pi}{\lambda_0} (x'u + y'v) \right] \exp \left[ -j \frac{\pi}{\lambda_0 r} \left( (x'w)^2 + (y'w)^2 + (x'v - y'u)^2 \right) \right] dx' dy' \quad (39)$$

that reduces to

$$\gamma_{mn}(r, u, v, w) \approx \exp \left[ -j \frac{\pi}{\lambda_0 r} \left( (x_m w)^2 + (y_n w)^2 + (x_m v - y_n u)^2 \right) \right] \times \exp \left[ j \frac{2\pi}{\lambda_0} (x_m u + y_n v) \right] \Delta_x \Delta_y \text{sinc} \left[ \frac{\pi \Delta_x}{\lambda_0} u \right] \text{sinc} \left[ \frac{\pi \Delta_y}{\lambda_0} v \right] \quad (40)$$

when using the approximation  $\exp \left[ -j \frac{\pi}{\lambda_0 r} \left( (x'w)^2 + (y'w)^2 + (x'v - y'u)^2 \right) \right] \approx \exp \left[ -j \frac{\pi}{\lambda_0 r} \left( (x_m w)^2 + (y_n w)^2 + (x_m v - y_n u)^2 \right) \right]$  since  $(x, y) \in \Omega_{mn}$ .

Finally, equation (20) is derived by substituting (40) in (37).

## Acknowledgements

This work benefited from the networking activities carried out within the Project ‘‘Cloaking Metasurfaces for a New Generation of Intelligent Antenna Systems (MANTLES)’’ (Grant No. 2017BHFZKH) funded by the Italian Ministry of Education, University, and Research under the PRIN2017 Program (CUP: E64I19000560001). Moreover, it benefited from the networking activities carried out within the Project ‘‘SPEED’’ (Grant No. 61721001) funded by National Science Foundation of China under the Chang-Jiang Visiting Professorship Program.

## References

- [1] M. Di Renzo, M. Debbah, D.-T. Phan-Huy, A. Zappone, M.-S. Alouini, C. Yuen, V. Sciancalepore, G. C. Alexandropoulos, J. Hoydis, H. Gacanin, J. De Rosny, A. Bounceur, G. Lerosey, and M. Fink, ‘‘Smart radio environments empowered by reconfigurable AI metasurfaces: An idea whose time has come,’’ *EURASIP J. Wireless Commun. Netw.*, vol. 129, pp. 1-20, 2019.

- [2] M. Di Renzo, A. Zappone, M. Debbah, M.-S. Alouini, C. Yuen, J. De Rosny, and S. Tretyakov, "Smart radio environments empowered by reconfigurable intelligent surfaces: How it works, state of research, and the road ahead," *IEEE J. Sel. Areas Comm.*, vol. 38, no. 11, pp. 2450-2525, Nov. 2020.
- [3] M. Di Renzo, K. Ntontin, J. Song, F. H. Danufane, X. Qian, F. Lazarakis, J. De Rosny, D.-T. Phan-Huy, O. Simeone, R. Zhang, M. Debbah, G. Lerosey, M. Fink, S. Tretyakov, and S. Shamai, "Reconfigurable intelligent surfaces vs. relaying: Differences, similarities, and performance comparison," *IEEE Open J. Comm. Soc.*, vol. 1, pp. 798-807, 2020.
- [4] A. Massa, A. Benoni, P. Da Ru, S. K. Goudos, B. Li, G. Oliveri, A. Polo, P. Rocca, and M. Salucci, "Designing smart electromagnetic environments for next-generation wireless communications," *Telecom*, vol. 2, no. 2, pp. 213-221, 2021.
- [5] G. Oliveri, P. Rocca, M. Salucci, and A. Massa, "Holographic smart EM skins for advanced beam power shaping in next generation wireless environments," *IEEE J. Multiscale Multiphysics Computat. Techn.*, vol. 6, pp. 171-182, Oct. 2021.
- [6] M. Salucci, G. Oliveri and A. Massa, "An innovative inverse source approach for the feasibility-driven design of reflectarrays," *IEEE Trans. Antennas Propag.*, to be published, DOI: 10.1109/TAP.2022.3161558.
- [7] P. Rocca, P. Da Ru, N. Anselmi, M. Salucci, G. Oliveri, D. Erricolo, and A. Massa, "On the design of modular reflecting EM skins for enhanced urban wireless coverage," *IEEE Trans. Antennas Propag.*, to be published, DOI: 10.1109/TAP.2022.3146870.
- [8] M. Barbuto, Z. Hamzavi-Zarghani, M. Longhi, A. Monti, D. Ramaccia, S. Vellucci, A. Toscano, and F. Bilotti, "Metasurfaces 3.0: a New Paradigm for Enabling Smart Electromagnetic Environments," *IEEE Trans. Antennas Propag.*, to be published, DOI: 10.1109/TAP.2021.3130153.
- [9] A. Benoni, M. Salucci, G. Oliveri, P. Rocca, B. Li, and A. Massa, "Planning of EM skins for improved quality-of-service in urban areas," *IEEE Trans. Antennas Propag.*, to be published, DOI: 10.1109/TAP.2022.3177284.

- [10] D. Dardari, N. Decarli, A. Guerra, and F. Guidi, "LOS/NLOS Near-Field Localization with a Large Reconfigurable Intelligent Surface," *IEEE Trans. Wireless Comm.*, to be published, DOI: 10.1109/TWC.2021.3128415.
- [11] H. Yang, X. Yuan, J. Fang and Y.-C. Liang, "Reconfigurable intelligent surface aided constant-envelope wireless power transfer," *IEEE Trans. Sig. Process.*, vol. 69, pp. 1347-1361, 2021.
- [12] P. Mei, Y. Cai, K. Zhao, Z. Ying, G. F. Pedersen, X. Q. Lin, and S. Zhang, "On the Study of Reconfigurable Intelligent Surfaces in the Near-Field Region," *IEEE Trans. Antennas Propag.*, to be published, DOI: 10.1109/TAP.2022.3147533.
- [13] Y. Zhang, J. Zhang, M. Di Renzo, H. Xiao, and B. Ai, "Reconfigurable Intelligent Surfaces With Outdated Channel State Information: Centralized vs. Distributed Deployments," *IEEE Trans. Comm.*, vol. 70, no. 4, pp. 2742-2756, Apr. 2022.
- [14] F. H. Danufane, M. D. Renzo, J. de Rosny, and S. Tretyakov, "On the path-loss of Reconfigurable Intelligent Surfaces: An approach based on Green's theorem applied to vector fields," *IEEE Trans. Comm.*, vol. 69, no. 8, pp. 5573-5592, Aug. 2021.
- [15] C. A. Balanis, *Antenna Theory: Analysis and Design*, 2nd ed. New York: Wiley, 1997.
- [16] A. Diaz-Rubio and S. A. Tretyakov, "Macroscopic modeling of anomalously reflecting metasurfaces: Angular response and far-field scattering," *IEEE Trans. Antennas Propag.*, vol. 69, no. 10, pp. 6560-6571, Oct. 2021.
- [17] F. Yang and Y. Rahmat-Samii, *Surface Electromagnetics with Applications in Antenna, Microwave, and Optical Engineering*, Cambridge, UK: Cambridge University Press, 2019.
- [18] ANSYS Electromagnetics Suite - HFSS (2021). ANSYS, Inc.
- [19] G. Oliveri, F. Zardi, P. Rocca, M. Salucci, and A. Massa, "Building a smart EM environment - AI-Enhanced aperiodic micro-scale design of passive EM skins," *IEEE Trans. Antennas Propag.*, to be published, DOI: 10.1109/TAP.2022.3151354.

- [20] A. Massa and M. Salucci, "On the design of complex EM devices and systems through the system-by-design paradigm - A framework for dealing with the computational complexity," *IEEE Trans. Antennas Propag.*, vol. 70, no. 2, pp. 1328-1343, Feb. 2022.
- [21] R. J. Mailloux, *Phased Array Antenna Handbook*, 2nd ed. Norwood, MA: Artech House, 2005.



## FIGURE CAPTIONS

- **Figure 1.** *Problem geometry.* Sketch of (a) the problem scenario, (b) the coordinate system, (c) the *EMS* meta-atom, and (d) the TX/RX horn antenna.
- **Figure 2.** *Numerical Study* ( $r_{TX} = 50$  [m]) - Plots of (a)(c) the magnitude and (b)(d) the phase distributions of the incident  $y$ -polarized electric field,  $F_{inc,y}^e(\mathbf{r})$ , generated on the *EMS* aperture,  $\Omega$ , by a transmitting horn antenna with gain (a)(b)  $G_{TX}^{\max} = 20.4$  [dBi] or (c)(d)  $G_{TX}^{\max} = 13.7$  [dBi].
- **Figure 3.** *Numerical Study* - Pictures of the *EMS* layout when (a)  $M \times N = 48 \times 48$  ( $\rightarrow \mathcal{L} \approx 0.41$  [m]) and  $\Delta l = 5.0 \times 10^{-3}$  [m] and (b)(c)  $M \times N = 84 \times 84$  ( $\rightarrow \mathcal{L} = 0.72$  [m]).
- **Figure 4.** *EMS-Analysis Validation* ( $G_{TX}^{\max} = 20.4$  [dBi],  $r_{TX} = 50$  [m],  $(\theta_{TX}, \varphi_{TX}) = (30, 180)$  [deg];  $M \times N = 48 \times 48 \rightarrow \mathcal{L} \approx 0.41$  [m],  $\Delta l = 5.0 \times 10^{-3}$  [m]) - Plots of  $|F_{ref,\varphi}^e(\mathbf{r})|$  in (a)(b)(c)  $\mathbf{r} \in \Theta_{NF}$  ( $r = 6$  [m],  $\theta = 30$  [deg]) or (d)(e)(f)  $\mathbf{r} \in \Theta_{FF}$  ( $r = 40$  [m],  $\theta = 30$  [deg]) predicted with (a)(d) the *FF* radiation theory [15], (b)(e) the generalized theory (20), and (c)(f) *HFSS*-computed.
- **Figure 5.** *EMS-Analysis Validation* ( $G_{TX}^{\max} = 20.4$  [dBi],  $r_{TX} = 50$  [m],  $(\theta_{TX}, \varphi_{TX}) = (30, 180)$  [deg];  $M \times N = 48 \times 48 \rightarrow \mathcal{L} \approx 0.41$  [m],  $\Delta l = 5.0 \times 10^{-3}$  [m]) - Plots of  $\Delta F_{ref,\varphi}^e(\mathbf{r})$  in (a)(b)  $\mathbf{r} \in \Theta_{NF}$  ( $r = 6$  [m],  $\theta = 30$  [deg]) or (c)(d)  $\mathbf{r} \in \Theta_{FF}$  ( $r = 40$  [m],  $\theta = 30$  [deg]) when using (a)(c) the *FF* radiation theory [15] or (b)(d) the generalized theory (20).
- **Figure 6.** *EMS-Analysis Validation* ( $G_{TX}^{\max} = 20.4$  [dBi],  $r_{TX} = 50$  [m],  $(\theta_{TX}, \varphi_{TX}) = (30, 180)$  [deg];  $M \times N = 84 \times 84 \rightarrow \mathcal{L} = 0.72$  [m];  $\mathbf{r} \in \Theta_{NF}$  ( $r = 10.5$  [m],  $\theta = 10$  [deg])) - Plots of  $\Delta F_{ref,\varphi}^e(\mathbf{r})$  for (a)(b) the layout in Fig. 3(b) or (c)(d) the layout in Fig. 3(c) when using (a)(c) the *FF* radiation theory [15] or (b)(d) the generalized theory (20).
- **Figure 7.** *EMS-Analysis Validation* ( $G_{TX}^{\max} = 20.4$  [dBi],  $r_{TX} = 50$  [m],  $(\theta_{TX}, \varphi_{TX}) = (30, 180)$  [deg];  $M \times N = 84 \times 84 \rightarrow \mathcal{L} = 0.72$  [m];  $\mathbf{r} \in \Theta_{FF}$  ( $r = 121$  [m],  $\theta = 10$  [deg])) - Plots of  $\Delta F_{ref,\varphi}^e(\mathbf{r})$  for (a)(b) the layout in Fig. 3(b) or (c)(d) the layout in Fig. 3(c) when using (a)(c) the *FF* radiation theory [15] or (b)(d) the generalized theory (20).

- **Figure 8.** *EMS-Synthesis Assessment* ( $G_{TX}^{\max} = G_{RX}^{\max} = 13.7$  [dBi],  $r_{TX} = 50$  [m],  $(\theta_{TX}, \varphi_{TX}) = (30, 180)$  [deg];  $r_{RX} = 15$  [m],  $\theta_{RX} = 10$  [deg];  $M \times N = 120 \times 120 \rightarrow \mathcal{L} \approx 1.029$  [m]) - Plots of the distributions of (a)(b)  $arg [\tilde{J}_y^e(\mathbf{r})]$  and (c)(d)  $arg [J_y^e(\mathbf{r})]$  on the EMS aperture,  $\Omega$ , when applying (a)(c) the FFM or (b)(d) the USM along with (e) the cumulative distribution function of the phase mismatch,  $|\Delta J_y^e(\mathbf{r})|$ .
- **Figure 9.** *EMS-Synthesis Assessment* ( $G_{TX}^{\max} = G_{RX}^{\max} = 13.7$  [dBi],  $r_{TX} = 50$  [m],  $(\theta_{TX}, \varphi_{TX}) = (30, 180)$  [deg];  $r_{RX} = 15$  [m],  $\theta_{RX} = 10$  [deg];  $M \times N = 120 \times 120 \rightarrow \mathcal{L} \approx 1.029$  [m]) - Plots of (a)(b) the EMS layout and of (c)(d)  $|F_{ref,\varphi}^e(\mathbf{r})|$  in the receiver region  $\Theta_{RX}$  when applying (a)(c) the FFM or (b)(d) the USM.
- **Figure 10.** *EMS-Synthesis Assessment* ( $G_{TX}^{\max} = G_{RX}^{\max} = 13.7$  [dBi],  $r_{TX} = 50$  [m],  $(\theta_{TX}, \varphi_{TX}) = (30, 180)$  [deg];  $\theta_{RX} = 10$  [deg];  $M \times N = 120 \times 120 \rightarrow \mathcal{L} \approx 1.029$  [m]) - Behavior of  $\Psi_{RX}$  versus the receiver distance  $r_{RX}$ .
- **Figure 11.** *EMS-Synthesis Assessment* ( $G_{TX}^{\max} = G_{RX}^{\max} = 13.7$  [dBi],  $r_{TX} = 50$  [m],  $(\theta_{TX}, \varphi_{TX}) = (30, 180)$  [deg];  $\theta_{RX} = 10$  [deg]) - Color-maps in the parametric domain  $(\mathcal{L}, r_{RX}) = (1.03 \times 10^{-1} \text{ [m]} \leq \mathcal{L} \leq 2.057 \text{ [m]} \rightarrow 12 \times 12 \leq M \times N \leq 240 \times 240; 30 \text{ [m]} \leq r_{RX} \leq 150 \text{ [m]})$  of (a)(b) the value of the power  $\Psi_{RX}$  when applying (a) the FFM or (b) the USM and of (c) corresponding  $\Delta\Psi_{RX}$  values.
- **Figure 12.** *EMS-Synthesis Assessment* ( $G_{TX}^{\max} = G_{RX}^{\max} = 13.7$  [dBi],  $r_{TX} = 50$  [m],  $(\theta_{TX}, \varphi_{TX}) = (30, 180)$  [deg];  $r_{RX} = 30$  [m],  $\theta_{RX} = 10$  [deg];  $M \times N = 240 \times 240 \rightarrow \mathcal{L} = 2.057$  [m]) - Plots of (a)(b) the EMS layout and of (c)(d)  $|F_{ref,\varphi}^e(\mathbf{r})|$  in the receiver region  $\Theta_{RX}$  when applying (a)(c) the FFM or (b)(d) the USM.
- **Figure 13.** *EMS-Synthesis Assessment* ( $G_{TX}^{\max} = G_{RX}^{\max} = 13.7$  [dBi];  $r_{TX} = 50$  [m],  $(\theta_{TX}, \varphi_{TX}) = (30, 180)$  [deg];  $r_{RX} = 15$  [m];  $M \times N = 120 \times 120 \rightarrow \mathcal{L} \approx 1.029$  [m]) - Plots of (a) the behavior of  $\Psi_{RX}$  versus  $r_{RX}$  when  $\theta_{RX} \in \{0, 30, 50\}$  [deg] and pictures of (a)(b) the EMS layouts synthesized when (b)(d)  $\theta_{RX} = 30$  [deg] or (c)(e)  $\theta_{RX} = 50$  [deg] with (b)(c) the FFM or (d)(e) the USM.
- **Figure 14.** *EMS-Synthesis Assessment* ( $G_{TX}^{\max} = G_{RX}^{\max} = 13.7$  [dBi];  $r_{TX} = 50$  [m],

$(\theta_{TX}, \varphi_{TX}) = (30, 180)$  [deg];  $r_{RX} = 15$  [m];  $M \times N = 120 \times 120 \rightarrow \mathcal{L} \approx 1.029$  [m])

- Plots of  $|F_{ref,\varphi}^e(\mathbf{r})|$  reflected in the receiver region  $\Theta_{RX}$  when (a)(c)  $\theta_{RX} = 30$  [deg] or (b)(d)  $\theta_{RX} = 50$  [deg] by the EMS synthesized with (a)(b) the FFM [Figs. 13(b)-13(c)] or (b)(d) the USM [Figs. 13(d)-13(e)].

- **Figure 15.** EMS-Synthesis Assessment ( $G_{TX}^{\max} = G_{RX}^{\max} = 13.7$  [dBi];  $(\theta_{TX}, \varphi_{TX}) = (30, 180)$  [deg];  $\theta_{RX} = 10$  [deg];  $M \times N = 120 \times 120 \rightarrow \mathcal{L} \approx 1.029$  [m]) - Plots of (a) the behavior of  $\Psi_{RX}$  versus  $r_{RX}$  when  $r_{TX} \in \{15, 100\}$  [m] and of (b)(c) the EMS layout along with (d)(e) the corresponding  $|F_{ref,\varphi}^e(\mathbf{r})|$  distribution in the receiver region  $\Theta_{RX}$  when setting  $r_{RX} = r_{TX} = 15$  [m] and using (b)(d) the FFM or (c)(e) the USM.
- **Figure 16.** EMS-Synthesis Assessment ( $G_{TX}^{\max} = G_{RX}^{\max} = 20.4$  [dBi],  $r_{TX} = 50$  [m],  $(\theta_{TX}, \varphi_{TX}) = (30, 180)$  [deg];  $M \times N = 120 \times 120 \rightarrow \mathcal{L} \approx 1.029$  [m]) - Behavior of  $\Psi_{RX}$  versus  $r_{RX}$  when  $\theta_{RX} \in \{10, 30, 50\}$  [deg].
- **Figure 17.** EMS-Synthesis Assessment ( $G_{TX}^{\max} = G_{RX}^{\max} = 20.4$  [dBi],  $r_{TX} = 50$  [m],  $(\theta_{TX}, \varphi_{TX}) = (30, 180)$  [deg];  $\theta_{RX} = 10$  [deg];  $M \times N = 84 \times 84 \rightarrow \mathcal{L} = 0.72$  [m]) - Comparison between the predicted and HFSS-computed values of  $\Delta\Psi_{RX}$  versus  $r_{RX}$ .

## TABLE CAPTIONS

- **Table I.** Numerical Study - Values of the descriptors of the horn antenna in Fig. 1(d).

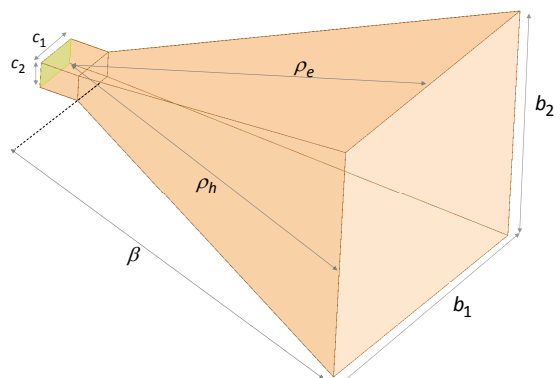
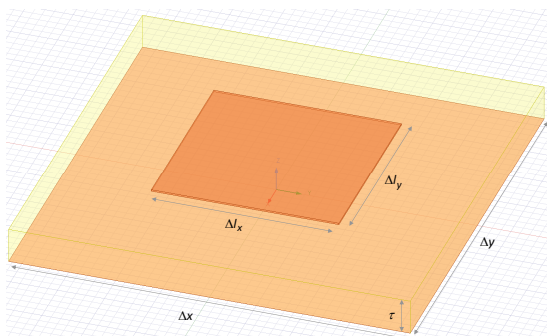
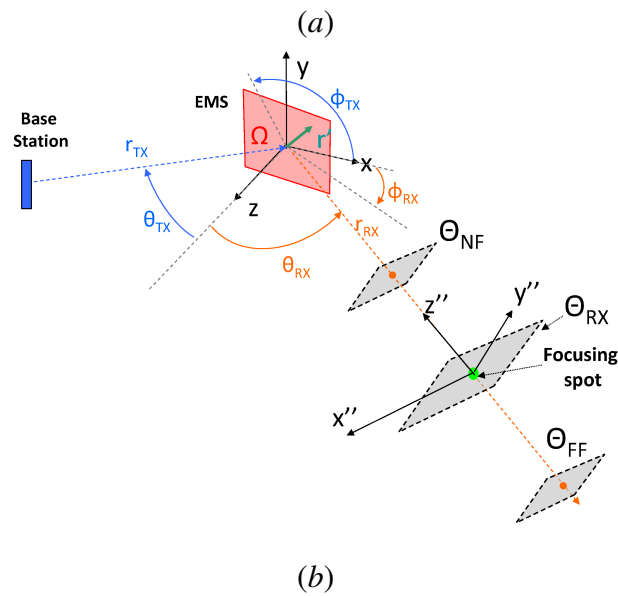
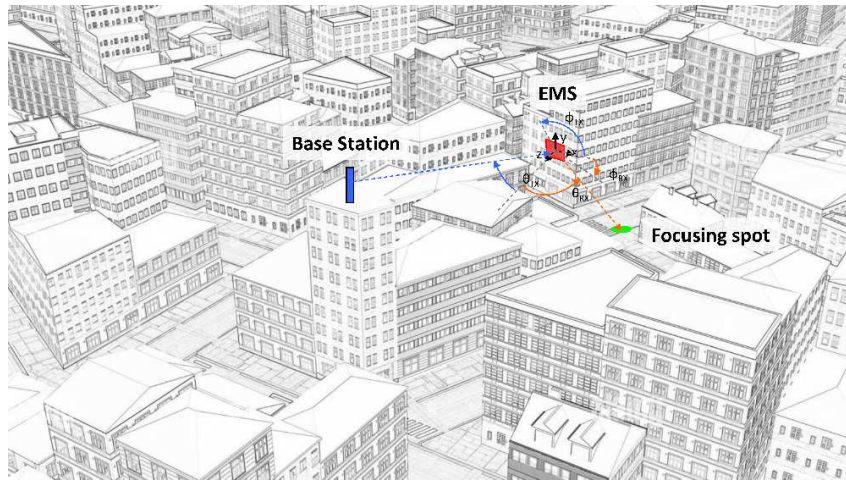
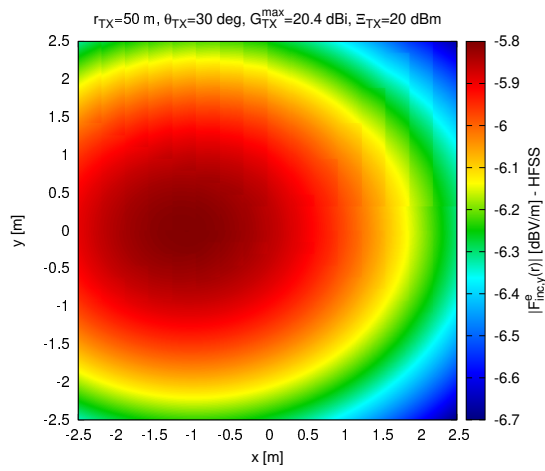
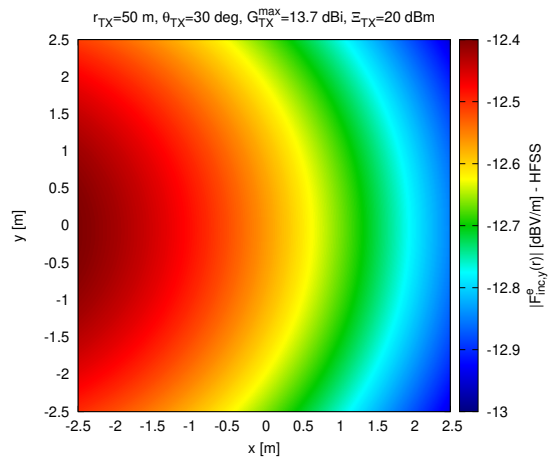


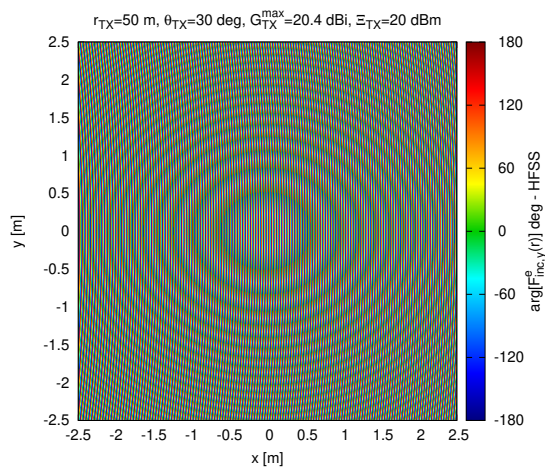
Fig. 1 - G. Oliveri et al., "Generalized Analysis and Unified Design of EM Skins ..."



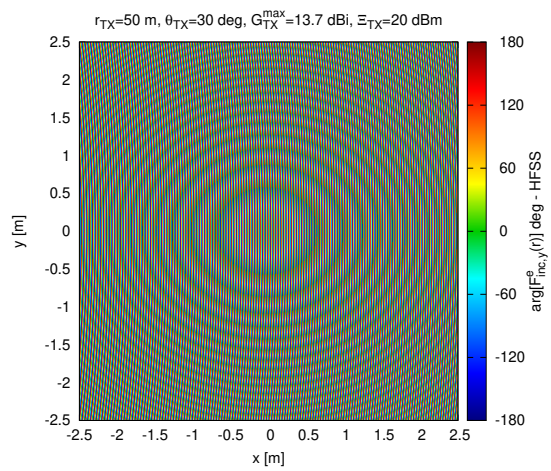
(a)



(c)

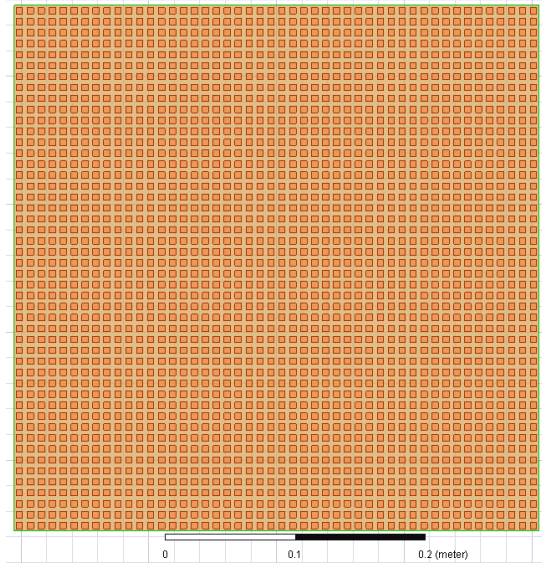


(b)

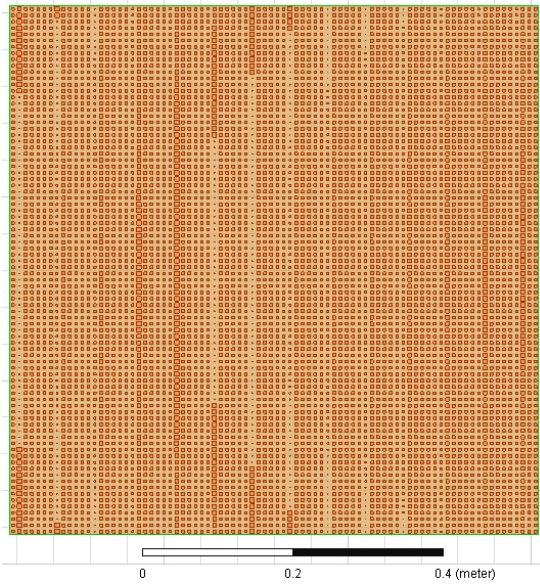


(d)

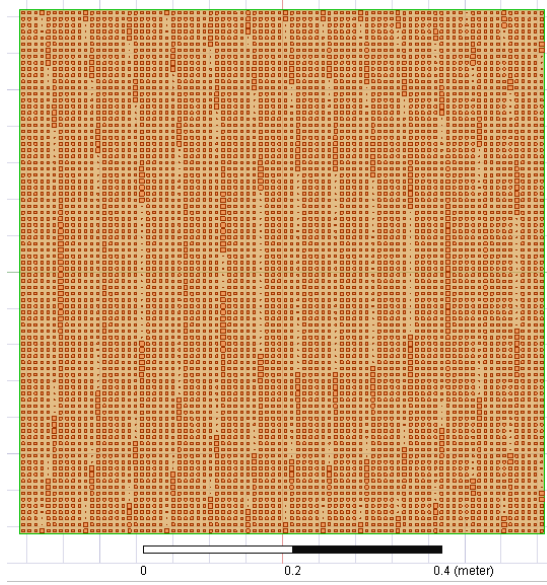
Fig. 2 - G. Oliveri et al., "Generalized Analysis and Unified Design of EM Skins ..."



(a)



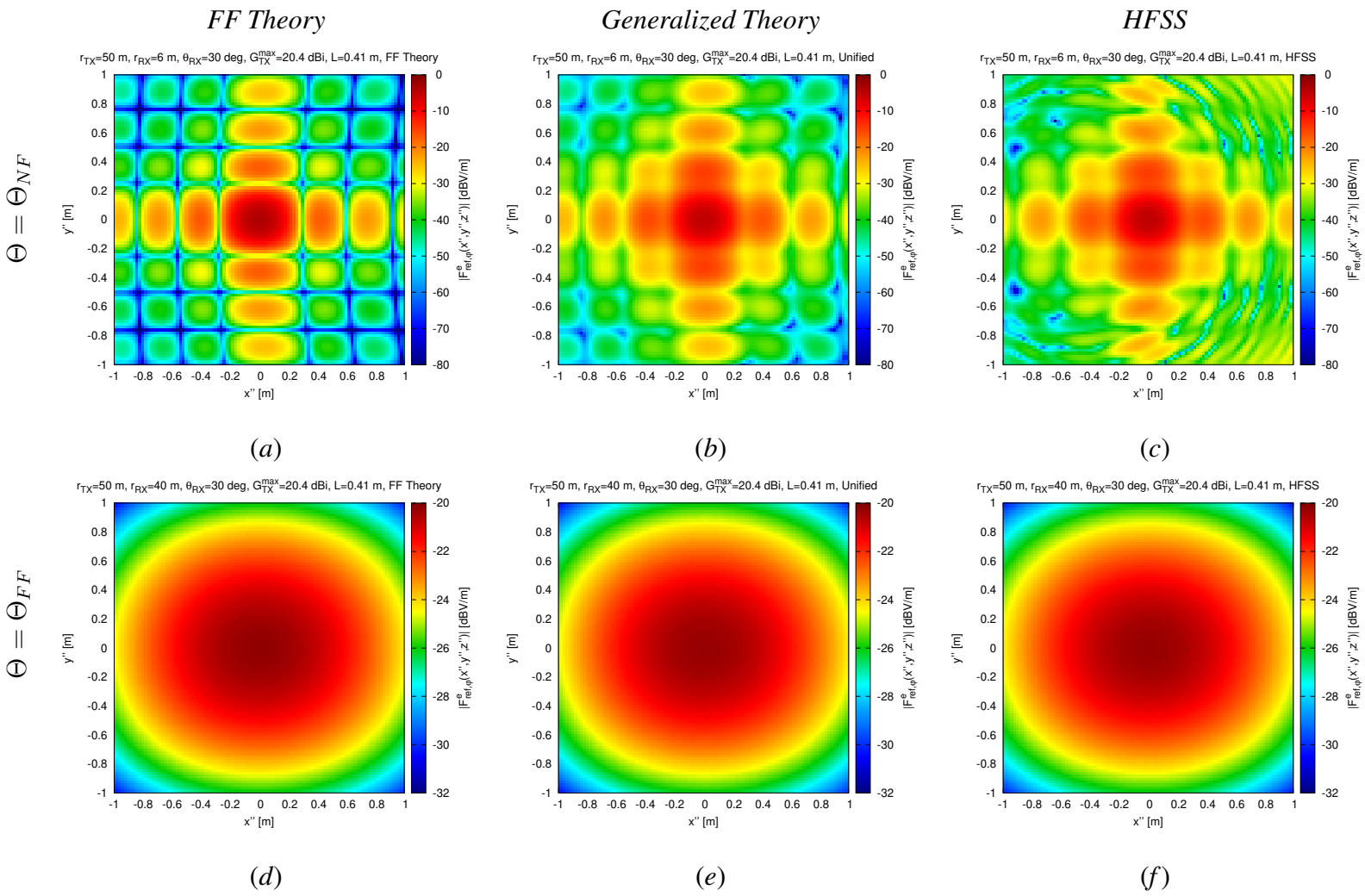
(b)



(c)

Fig. 3 - G. Oliveri et al., “Generalized Analysis and Unified Design of *EM* Skins ...”

Fig. 4 - G. Oliveri et al., "Generalized Analysis and Unified Design of EM Skins ..."



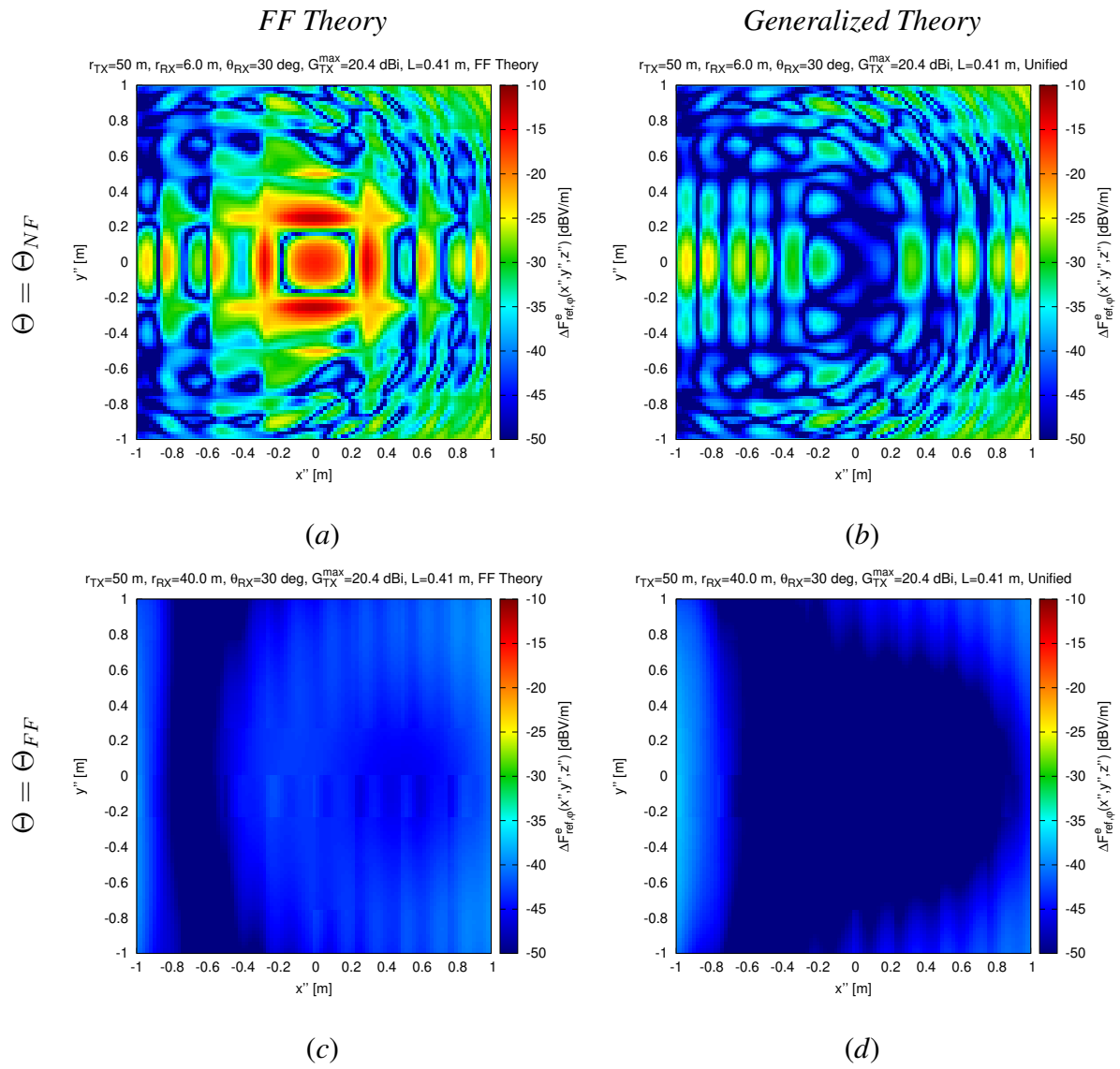


**Fig. 5 - G. Oliveri et al., “Generalized Analysis and Unified Design of EM Skins ...”**



$$\Theta = \Theta_{NF}$$

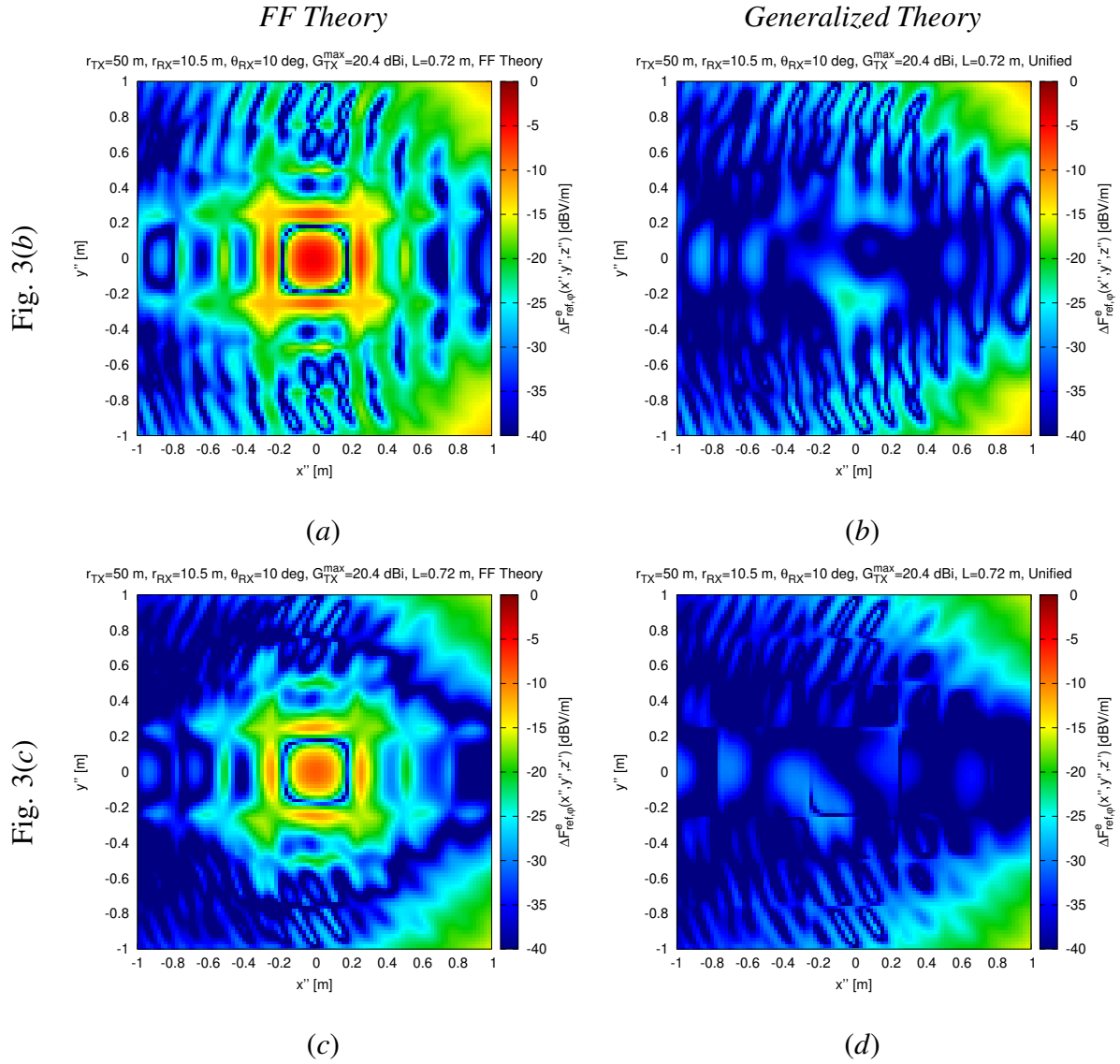


Fig. 6 - G. Oliveri et al., “Generalized Analysis and Unified Design of EM Skins ...”

$$\Theta = \Theta_{FF}$$

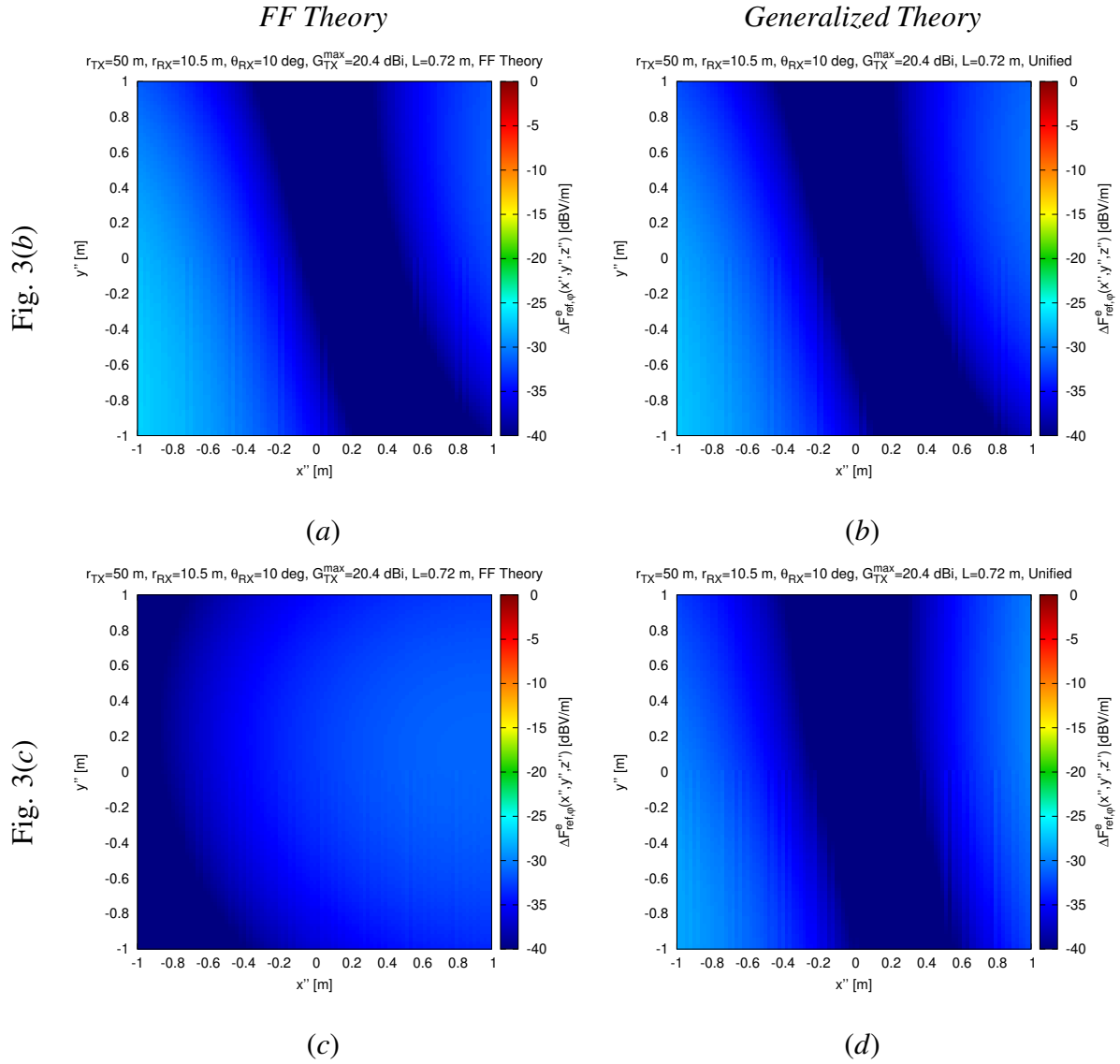
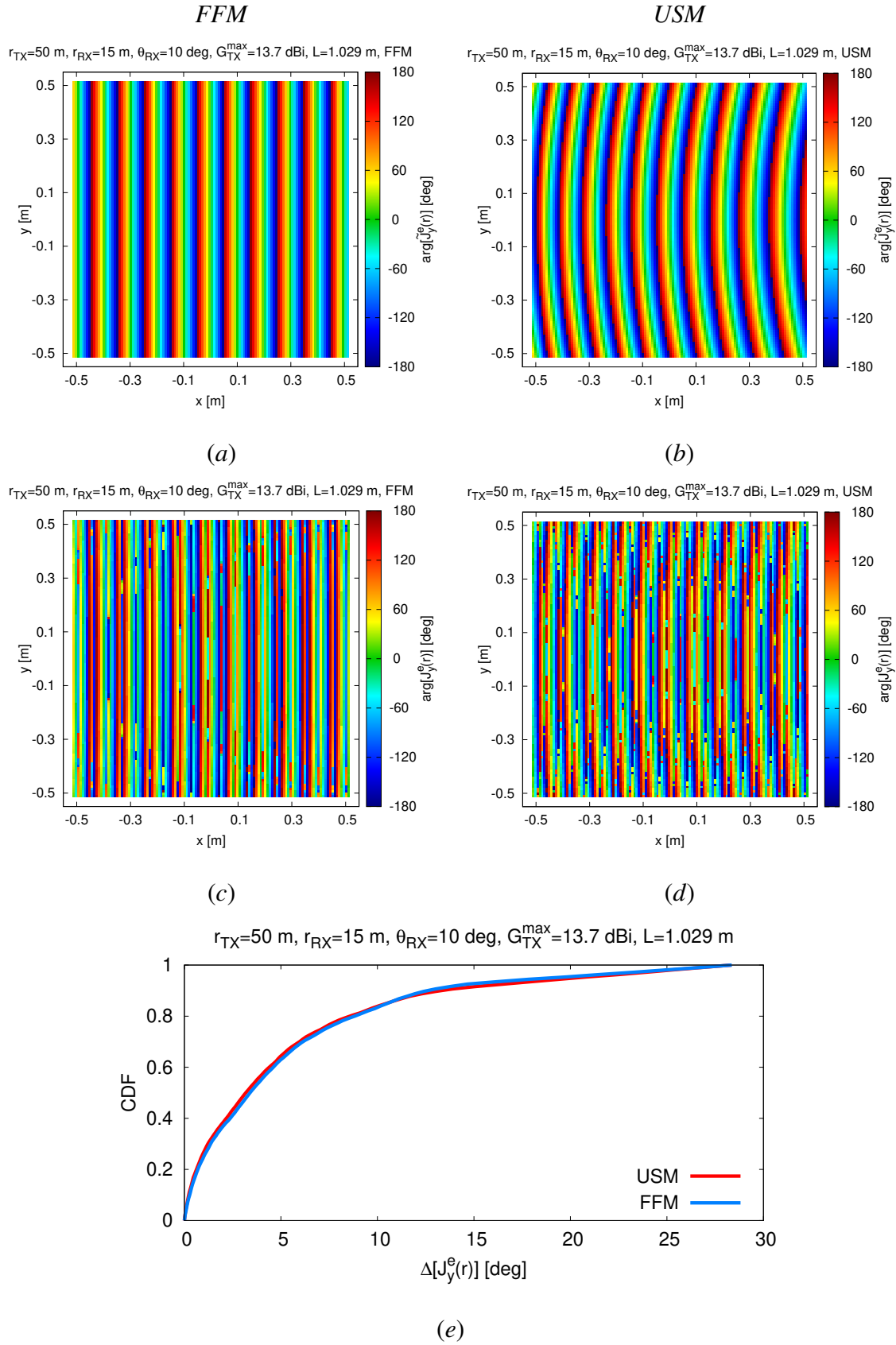


Fig. 7 - G. Oliveri et al., “Generalized Analysis and Unified Design of EM Skins ...”



**Fig. 8 - G. Oliveri et al., “Generalized Analysis and Unified Design of EM Skins ...”**

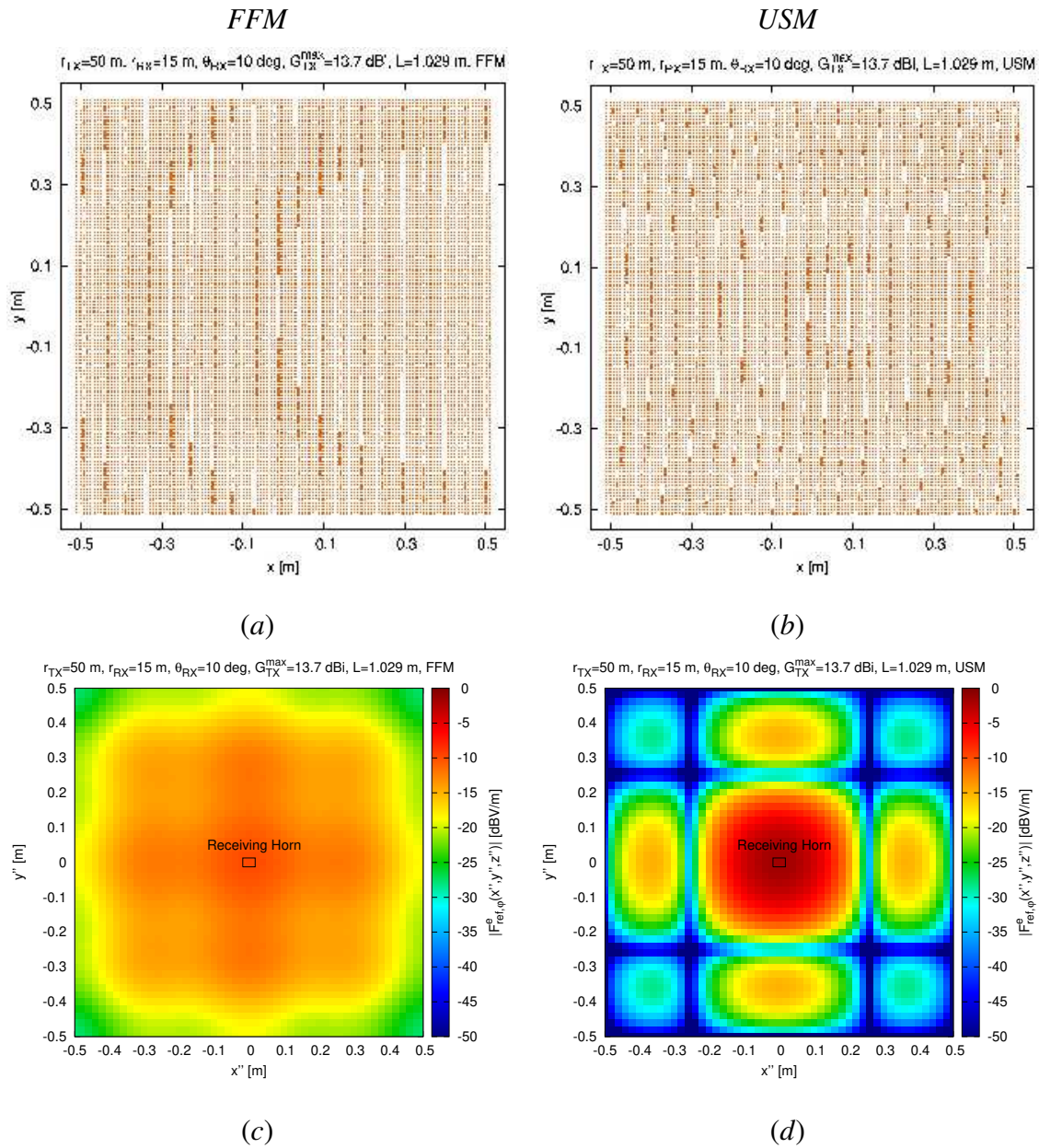
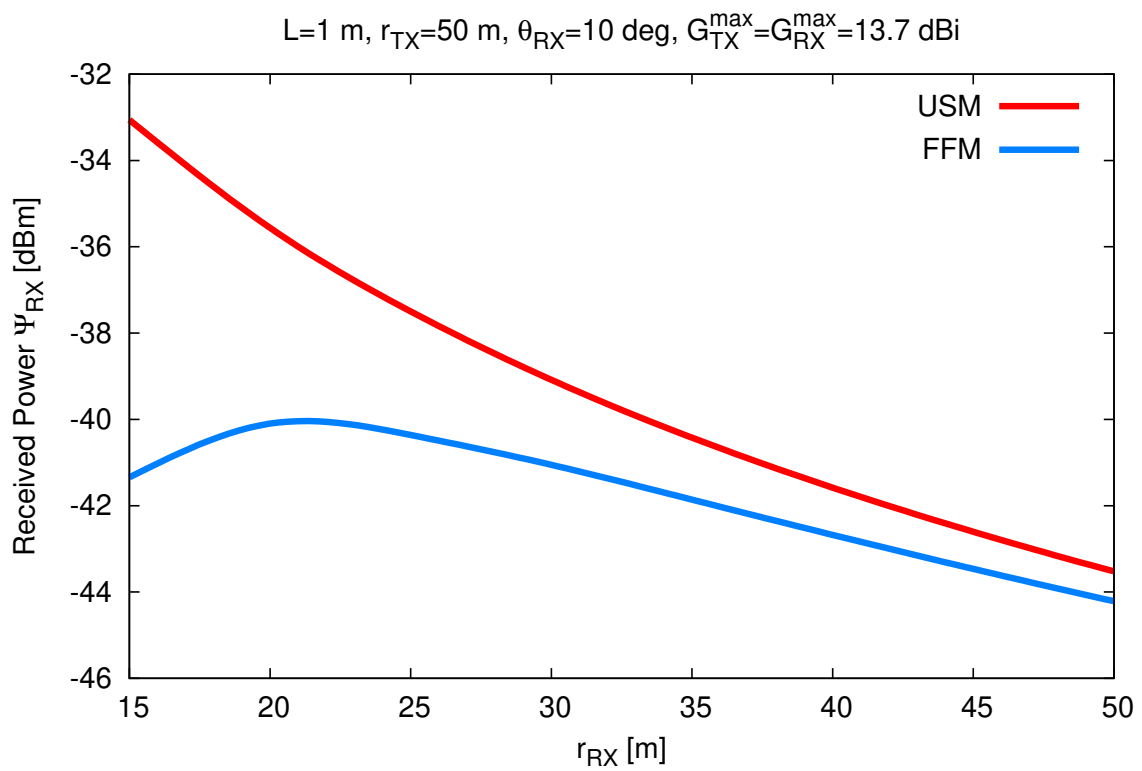
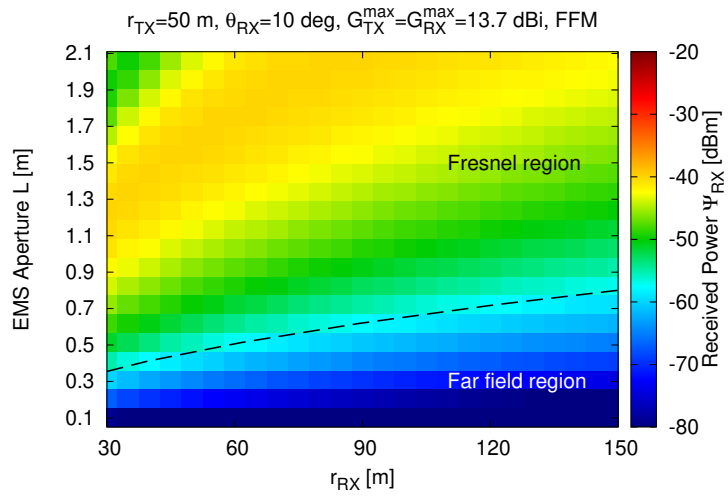


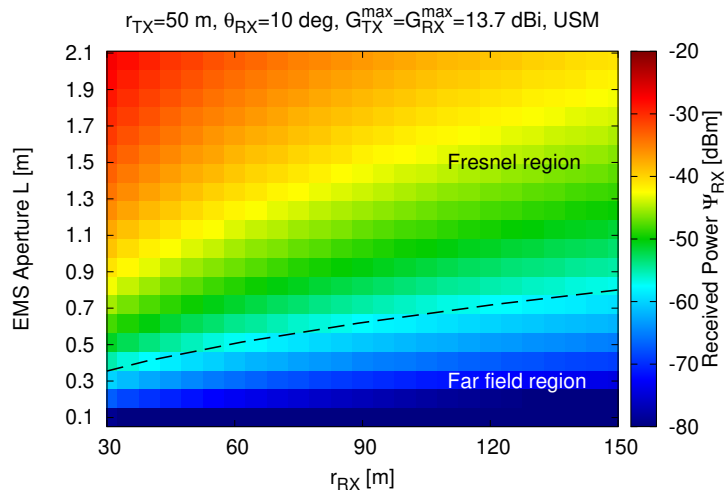
Fig. 9 - G. Oliveri et al., "Generalized Analysis and Unified Design of EM Skins ..."



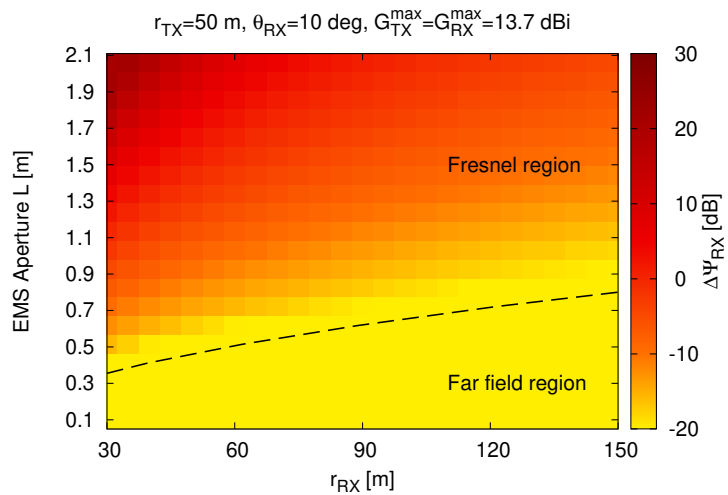
**Fig. 10 - G. Oliveri et al., “Generalized Analysis and Unified Design of EM Skins ...”**



(a)



(b)



(c)

Fig. 11 - G. Oliveri et al., "Generalized Analysis and Unified Design of EM Skins ..."

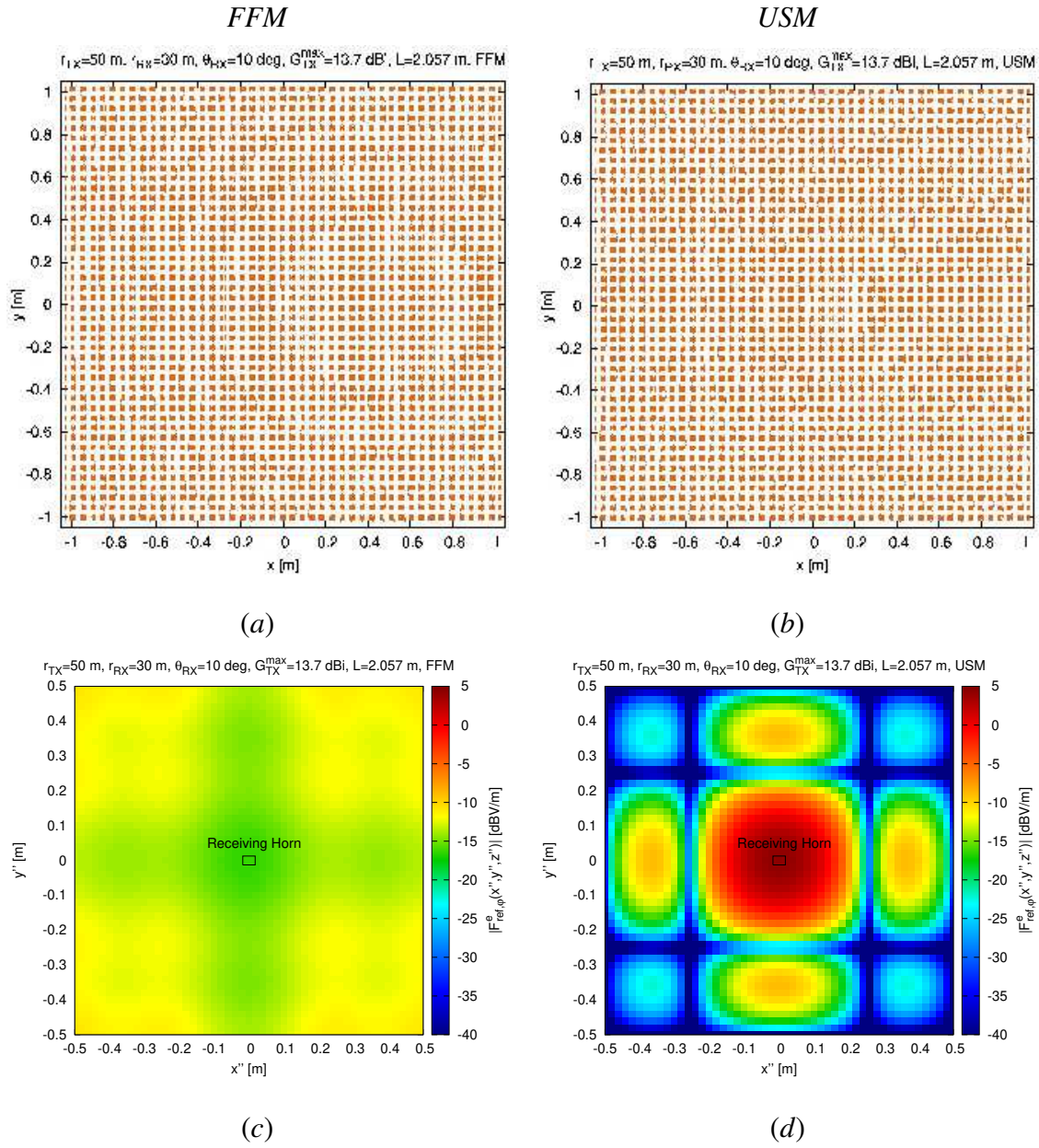
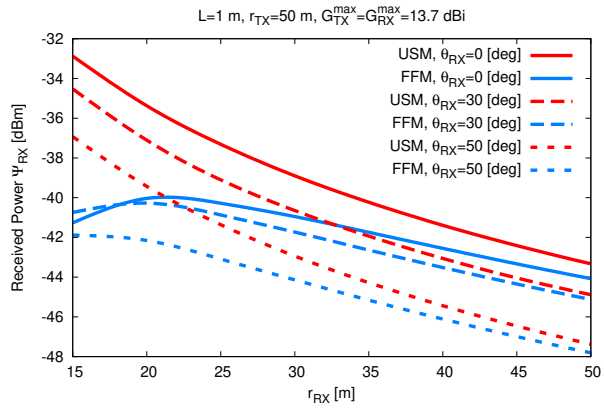


Fig. 12 - G. Oliveri et al., “Generalized Analysis and Unified Design of EM Skins ...”



(a)

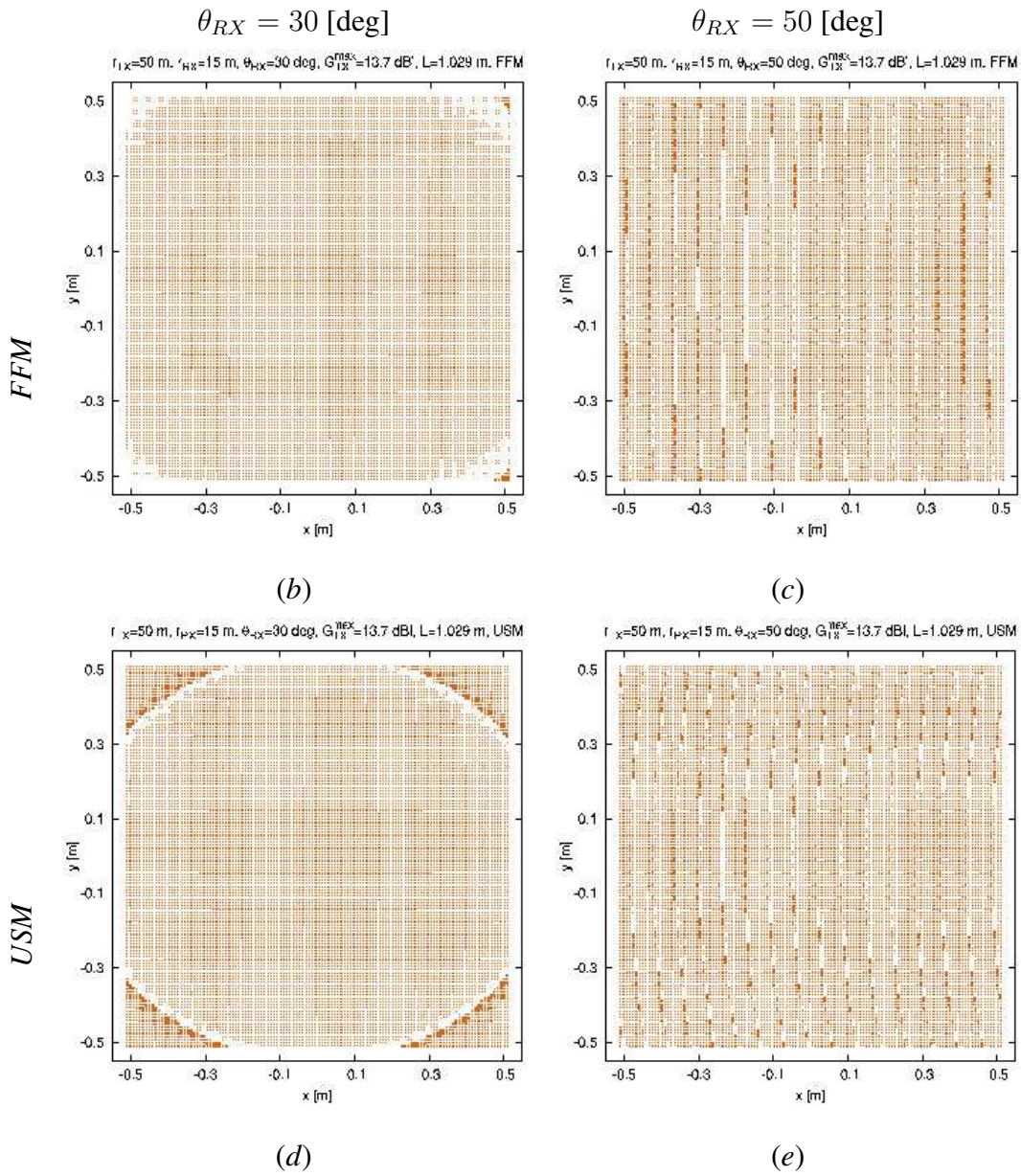
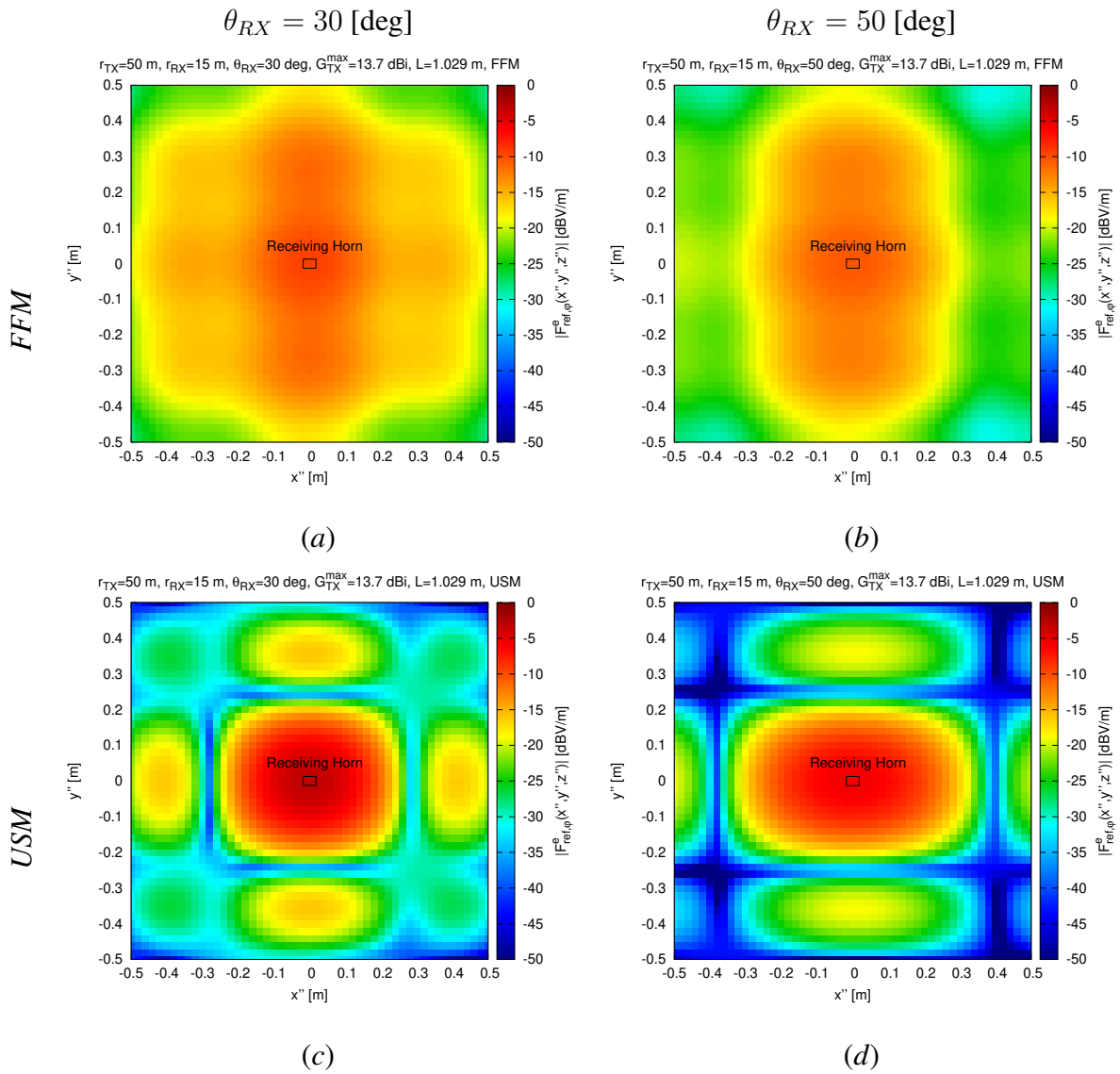
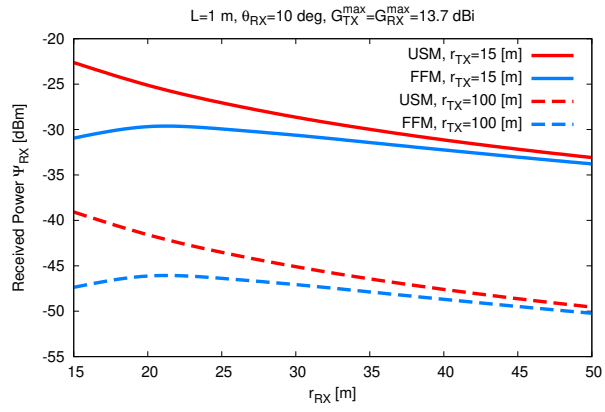


Fig. 13 - G. Oliveri et al., "Generalized Analysis and Unified Design of EM Skins ..."



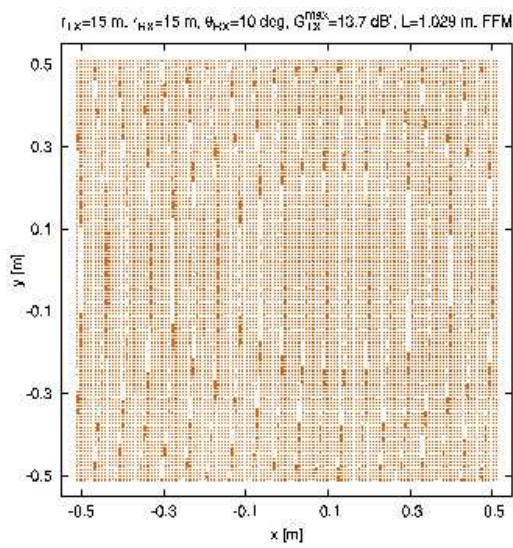


**Fig. 14 - G. Oliveri et al., “Generalized Analysis and Unified Design of EM Skins ...”**



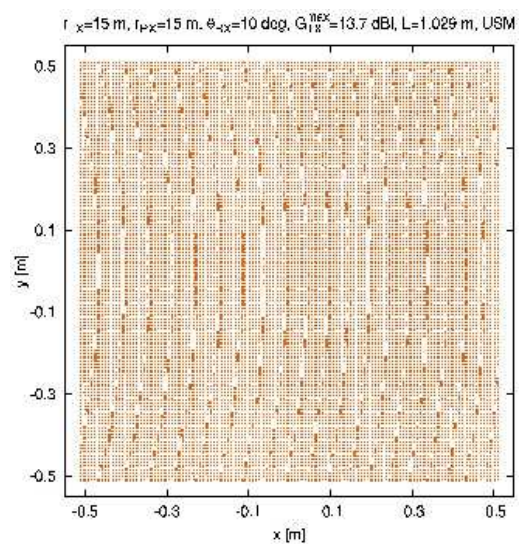
(a)

*FFM*

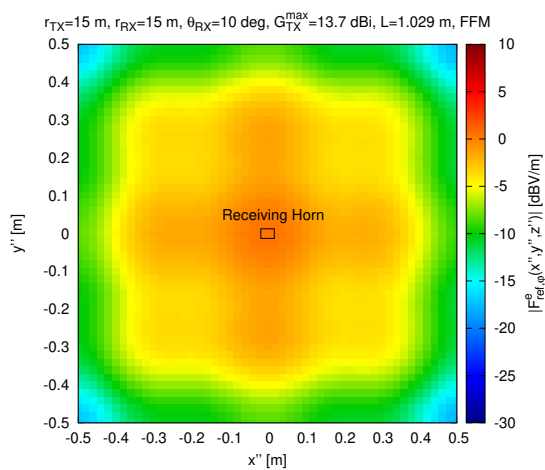


(b)

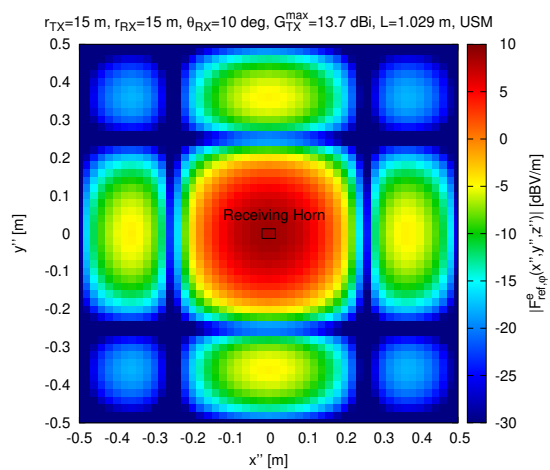
*USM*



(c)



(d)



(e)

**Fig. 15 - G. Oliveri et al., “Generalized Analysis and Unified Design of EM Skins ...”**

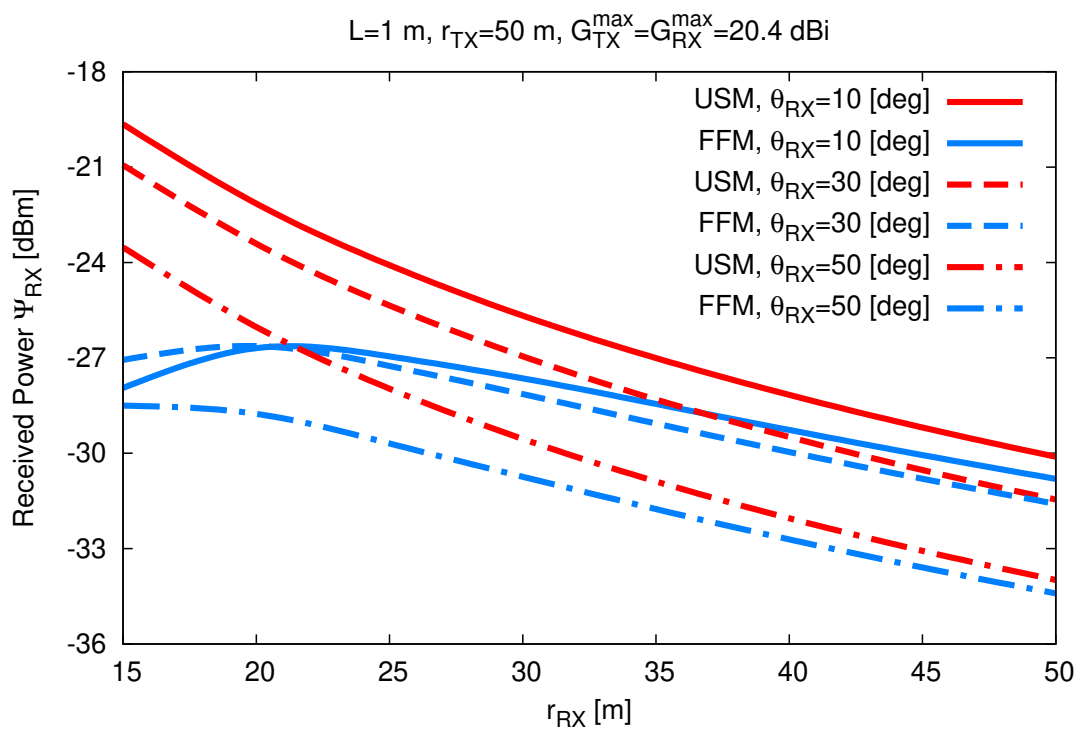


**Fig. 16 - G. Oliveri et al., “Generalized Analysis and Unified Design of EM Skins ...”**

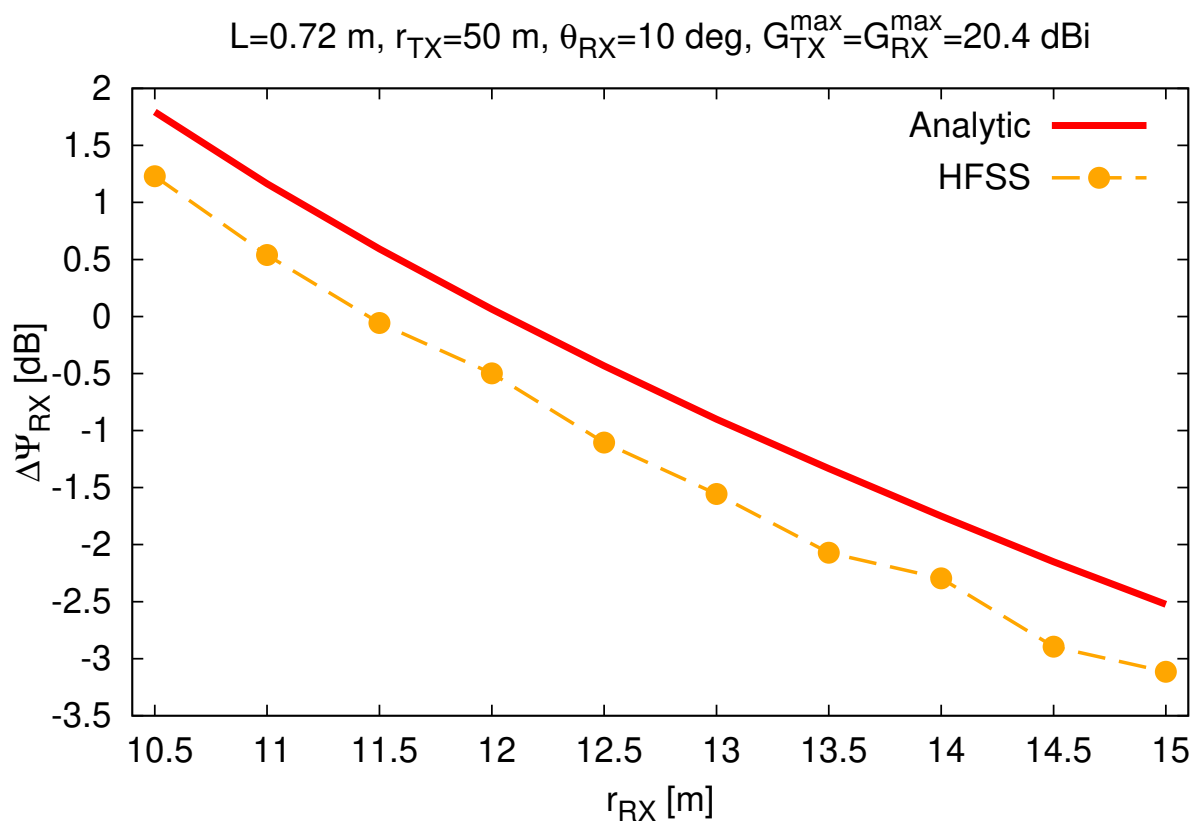


**Fig. 17 - G. Oliveri et al., “Generalized Analysis and Unified Design of *EM* Skins ...”**

	<b>Low-Gain Horn</b>	<b>High-Gain Horn</b>
$f$ [GHz]	17.5	17.5
$c_1$ [m]	$1.295 \times 10^{-2}$	$1.295 \times 10^{-2}$
$c_2$ [m]	$6.477 \times 10^{-3}$	$6.477 \times 10^{-3}$
$\beta$ [m]	$1.072 \times 10^{-3}$	$8.897 \times 10^{-2}$
$\rho_e$ [m]	$1.925 \times 10^{-2}$	$1.041 \times 10^{-1}$
$\rho_h$ [m]	$2.449 \times 10^{-2}$	$1.137 \times 10^{-1}$
$b_1$ [m]	$3.549 \times 10^{-2}$	$7.648 \times 10^{-2}$
$b_2$ [m]	$2.569 \times 10^{-2}$	$5.976 \times 10^{-2}$
$G^{\max}$ [dBi]	13.7	20.4

**Table I - G. Oliveri et al., “Generalized Analysis and Unified Design of *EM* Skins ...”**

This figure "Fig.3a.png" is available in "png" format from:

<http://arxiv.org/ps/2207.08419v1>

This figure "Fig.3b.png" is available in "png" format from:

<http://arxiv.org/ps/2207.08419v1>

This figure "Fig.3c.png" is available in "png" format from:

<http://arxiv.org/ps/2207.08419v1>